


Numerical modeling of hemodynamics scenarios of patient-specific coronary artery bypass grafts

Francesco Ballarin^{1,2}  · Elena Faggiano^{1,3} · Andrea Manzoni⁴ ·
Alfio Quarteroni⁴ · Gianluigi Rozza² · Sonia Ippolito⁵ · Carlo Antona⁶ ·
Roberto Scrofani⁶

Received: 6 October 2016 / Accepted: 27 February 2017 / Published online: 13 March 2017
© Springer-Verlag Berlin Heidelberg 2017

Abstract A fast computational framework is devised to the study of several configurations of patient-specific coronary artery bypass grafts. This is especially useful to perform a sensitivity analysis of the hemodynamics for different flow conditions occurring in native coronary arteries and bypass grafts, the investigation of the progression of the coronary artery disease and the choice of the most appropriate surgical procedure. A complete pipeline, from the acquisition of patient-specific medical images to fast parameterized computational simulations, is proposed. Complex surgical configurations employed in the clinical practice, such as Y-grafts and sequential grafts, are studied. A virtual surgery platform based on model reduction of unsteady Navier–Stokes equations for blood dynamics is proposed to carry out sensitivity analyses in a very rapid and reliable way. A specialized geometrical parameterization is employed to

compare the effect of stenosis and anastomosis variation on the outcome of the surgery in several relevant cases.

Keywords Cardiovascular simulations · Computational reduction strategies · Coronary bypass grafts · Patient-specific computing · Data assimilation · Geometrical parameterization

List of symbols

Coronary arteries of the right coronary tree

RCA	Right coronary artery
PDA	Posterior descending artery
PL	Postero-lateral artery

Coronary arteries of the left coronary tree

LCA	Main trunk of the left coronary artery
LAD	Left anterior descending artery
Diag.	Diagonal branch of the left anterior descending artery
LCX	Left circumflex artery
OM	Obtuse marginal artery

Bypass grafts

LITA	Left internal thoracic artery
Rad.	Radial artery bypass grafts
SVG	Saphenous vein bypass grafts

✉ Francesco Ballarin
francesco.ballarin@sissa.it

¹ Present Address: MOX - Modeling and Scientific Computing, Dipartimento di Matematica, Politecnico di Milano, P.za Leonardo da Vinci 32, 20133 Milan, Italy

² mathLab, Mathematics Area, SISSA, via Bonomea 265, 34136 Trieste, Italy

³ Present Address: Computational Mechanics and Advanced Materials Group, Department of Civil Engineering and Architecture, University of Pavia, Via Ferrata 3, 27100 Pavia, Italy

⁴ CMCS - Modelling and Scientific Computing, Ecole Polytechnique Fédérale de Lausanne, Station 8, 1015 Lausanne, Switzerland

⁵ Radiology Unit, Ospedale Luigi Sacco, Via G. B. Grassi 74, 20157 Milan, Italy

⁶ Cardiovascular Surgery Unit, Ospedale Luigi Sacco, Via G. B. Grassi 74, 20157 Milan, Italy

1 Introduction

Coronary artery bypass grafting (CABG) is a surgical procedure in which one or more grafts are used to restore blood flows to the myocardium when severe *coronary artery disease (CAD)* occurs. In this case, the occlusion of one or several major coronary arteries undermines the perfusion of oxygen-rich blood to the heart. Although several alternative treatments exist, CABG is still one of the most widespread surgical practice worldwide (Puskas et al. 2014). However, current clinical experience suggests that, after some years, the implanted vessels themselves tend to occlude due to the process of intimal thickening (see Fig. 1), leading to the failure of the surgery and ultimately to the need of reintervention (Puskas et al. 2014; Kirklin and Barratt-Boyes 1988; Go et al. 2014).

A vast clinical experience is available on this subject since the early attempts on CABG in the 50s: it concerns preliminary assessment of the disease, choices of the bypass grafts and anastomosis locations during surgery, and survey of clinical outcomes after surgery (Kirklin and Barratt-Boyes 1988). A better understanding of the hemodynamics in CABGs, both through experimental measurements and numerical simulations, has been achieved in the last decades, as summarized by several reviews (Ghista and Kabinejadian 2013; Migliavacca and Dubini 2005; Marsden 2014; Owida et al. 2012; Taylor and Draney 2004), dealing with either idealized (Fei et al. 1994; Inzoli et al. 1996) or patient-specific configurations (Frauenfelder et al. 2007; Dur et al. 2011; Sankaran et al. 2012). Parametric studies are of particular interest in order to assess the sensitivity of the intervention with respect to different physical conditions or surgical procedures, possibly leading to the proposal of new designs or the optimization of existing ones (Marsden 2014).

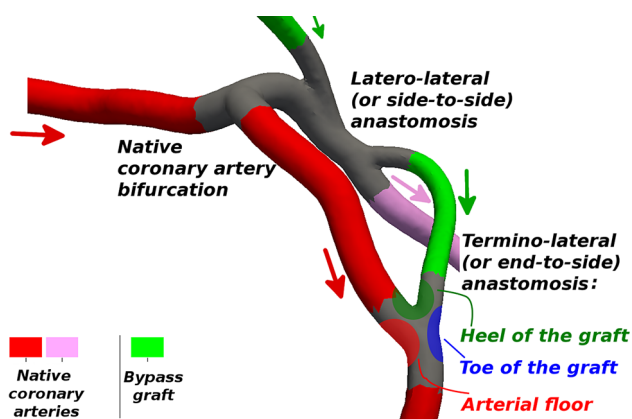


Fig. 1 Illustration of anastomosis (end-to-side and side-to-side) and bifurcations; intimal thickening of an end-to-side anastomosis typically occurs on the arterial floor and near the heel and toe of the graft. Arrows denote blood flow direction

Our aim is to apply the reduced order computational framework proposed in Ballarin et al. (2016) and Ballarin (2015) to several three-dimensional patient-specific CABG configurations, providing a virtual platform for the sensitivity analysis of blood flows for different surgical choices under different hemodynamic conditions, properly parameterized. The three key novelties in this work are concerned with: (i) the use of patient-specific geometries of complete, sequential bypass grafts, (ii) their integration in a parameterized framework to handle physical and, in particular, geometrical variations *without* any new segmentation or remeshing, by considering a small number of clinically relevant input parameters and (iii) their integration in a computational reduction framework to obtain numerical simulations for each new value of input parameters *without* querying expensive high-fidelity (e.g., finite element) solvers but using a reduced order solver relying on a reduced basis method. Indeed, the solution of expensive high-fidelity simulations requires order of a day even on modern high-performance computing architectures, while our proposed virtual platform allows to obtain a comparable solution (in terms of accuracy) in a few minutes, provided that an extensive offline stage of computations has been carried out once and for all. The main motivation behind the use of such virtual platform is that clinical interest is related not only to the simulation on a patient-specific configuration, but also to the need of addressing the variation of flow conditions and geometries to take into account several scenarios, aiming at a possible improvement of the design of the surgical operation and deeper comprehension of resulting flow conditions. Hence, the solution of expensive high-fidelity simulations for *each* new physical or geometrical configuration is usually unaffordable in terms of CPU time. This limitation can only be successfully overcome by relying on a reduced order methodology such as the one detailed in this work. This is why, in this paper, we apply the reduced model strategy proposed in Ballarin et al. (2016) and Ballarin (2015) to address several clinically relevant cases and rely on it to discuss and compare clinical outcomes of different surgical scenarios.

2 Materials and methods

Accurate numerical simulations of CABGs on patient-specific configurations in a wide range of scenarios are obtained in this work at greatly reduced computational costs thanks to the virtual surgery platform described in Ballarin et al. (2016). See also Fig. 2 for a graphical sketch. In this section we describe the proposed computational strategy, based on (i) medical imaging data, (ii) physical and geometrical parameterization to characterize different scenarios of interest and (iii) a projection-based reduced order model (ROM). We refer the reader to Hesthaven et al. (2016) and Quar-

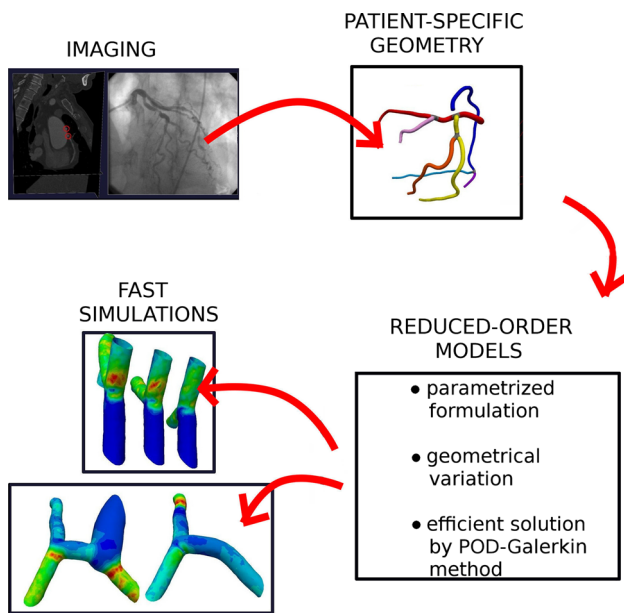


Fig. 2 A sketch of the proposed reduced order framework

teroni et al. (2016) for a detailed mathematical overview of the reduced basis method, which is the key computational tool ensuring substantial savings.

2.1 Patient-specific clinical dataset and medical imaging procedure

2.1.1 Patients recruitment and clinical data

Patients enrolled for this study have undergone CABG surgery due to critical coronary artery disease. Enrolled population features a broad variability of both disease and surgical intervention, with the aim of being representative of the most common cases. A summary of available clinical cases is provided in Fig. 3, Table 1. Internal review board approval was obtained to conduct this study.

For a better understanding of the surgery, each branch is denoted by a different color in Fig. 3. The right coronary tree is denoted by blue colors, while the left coronary tree is denoted by red/yellow colors. Grafts are colored with green tonalities. Table 1 summarizes surgical choices for each patient, related in particular to grafting materials (arterial grafts such as LITA or radial arteries, or venous grafts such as SVG) and their usage either as single or sequential grafts. LITA graft is employed in all patients, being the gold standard for the revascularization of the left coronary tree, and especially the LAD branch (Puskas et al. 2014). Patients differ widely on the remaining grafts, depending on the surgical choices related to the coronary artery disease. In all cases but one the disease affects two, three or more vessels; hence, more than one anastomosis is needed. In more than half of the patients, the number of required anastomoses is larger than

the available grafts, so that a sequential procedure is needed, in which a graft is used for more than one anastomosis. For each patient, the total number of bypasses is summarized in the last row of Table 1.

Available clinical data include both a pre-surgery angiographic study by means of a coronary angiography and a post-surgery computed tomography (CT) scan. A Toshiba angiography system is employed for the former, while a Philips Brilliance CT 64-slice system is employed to perform contrast enhanced CT, with a slice thickness of 0.67 mm, slice spacing of 0.4 mm, reconstruction matrix of 512×512 pixels, resolution of $0.3 \text{ mm} \times 0.3 \text{ mm} \times 0.3 \text{ mm}$. Acquisitions were carried out at approximately the 75% of the cardiac cycle, during which the heart is in the diastolic phase. This choice is motivated by the fact that in this phase coronary arteries are less stretched and more perfused by blood.

2.1.2 Medical imaging procedure

A medical imaging pipeline has been set up to build a mesh from CT scan clinical data, thanks to the integration with the Vascular Modelling Toolkit `vmtk` (Antiga et al. 2008). Anisotropic diffusion (Perona and Malik 1990) and vessel enhancement filters (Frangi et al. 1998) are applied to the CT scan image. A level set segmentation is then applied to the preprocessed image, as in Antiga (2002). The initialization of the level set is based on the *colliding front* method (Antiga et al. 2008). Once the level set segmentation is completed, a marching cube algorithm (Lorenson and Cline 1987) is employed to generate a polygonal surface. However, this may yield artifacts arising either from the CT scan data or the reconstruction procedure. For these reasons, we adopt a simplifying assumption and take advantage of the fact that both coronary arteries and bypass grafts are vessels of a network of tubular structures, and use the reconstructed geometry to extract the centerlines of these tubular structures. We refer to the centerline as to the curve $\gamma(s)$ connecting two outermost sections of the tentative geometry. The centerline $\gamma(s)$ locally maximizes the distance from the boundary of the vessel (Antiga 2002; Antiga et al. 2003, 2008). The value of the maximal inscribed radius $r(s)$ is also associated to each centerline point, where s denotes the curvilinear abscissa. A smoothing procedure is carried out (consisting of a running average on the coordinates, linearization of the radius with respect to the curvilinear abscissa), except near stenoses where data tabulated from angiography scan are employed to quantify the location and severity of the disease. Finally, the surface corresponding to each branch is obtained by sweeping a circular cross section of radius $r(s)$ along the centerlines $\gamma(s)$, and the interior of the resulting network is filled with volumetric elements in order to obtain a tetrahedral volume mesh using *TetGen* (Si 2015). In particular, a radius adaptive mesh is generated.

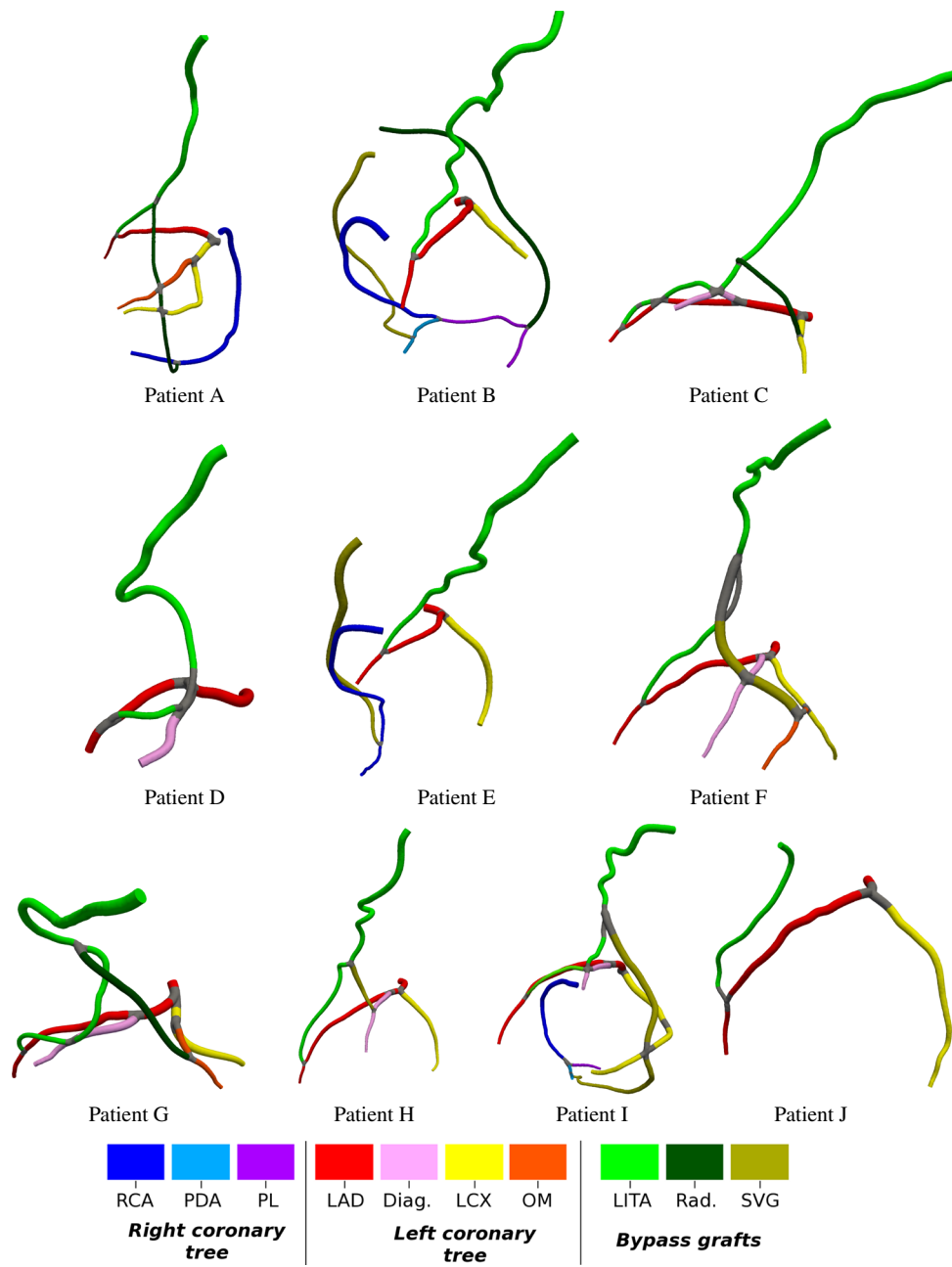


Fig. 3 Current clinical dataset

Table 1 Overview of the CABG surgery performed for each patient

	A	B	C	D	E	F	G	H	I	J
Single LITA graft	1	1			1	1		1		1
Single Rad. graft		1								
Single SVG graft		1			1					
Y-graft with LITA, single Rad. graft			1				1			
Y-graft with LITA, single SVG graft								1		
Sequential LITA grafts			3	2			2		2	
Y-graft with LITA, sequential Rad. grafts	3									
Y-graft with LITA, sequential SVG grafts						2			2	
Total number of bypass grafts	4	3	4	2	2	3	3	2	4	1

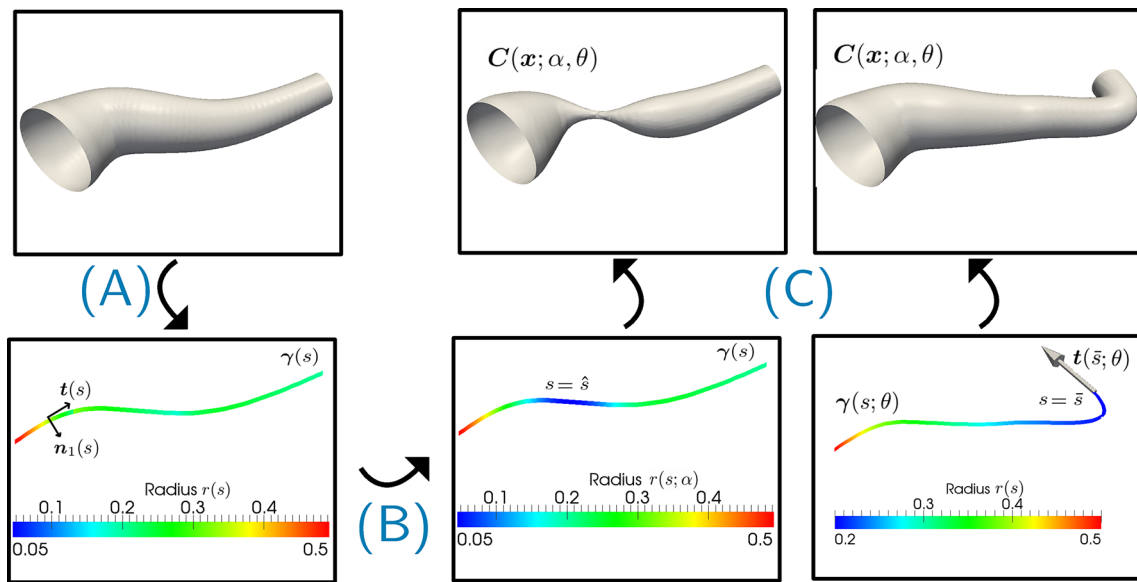


Fig. 4 A centerline-based parameterization (single curve)

2.2 Geometrical and physical parameterization

2.2.1 Geometrical parameterization for vascular vessels

In this work we consider two geometrical parameters, due to their clinical relevance for the problem at hand:

- *stenosis severity* α . This is a clinically relevant geometrical parameter; indeed, current experience suggests that surgery should be performed only for critical occlusions (Rowe et al. 1969; Hillis and Smith 2011; Sabik et al. 2005, 2003; Swillens et al. 2012). We use the virtual platform to vary stenosis factors in the range $[0, 90\%]$ in order to compare critical cases ($\alpha_j \geq 70\%$) to non-critical ones ($\alpha_j < 70\%$). The location of the stenosis and the extension of the stenotic region are kept fixed from the available clinical data. In case of double- or triple-vessel coronary artery disease, each stenosis is described by a single parameter α_j , where j denotes the stenosed artery (e.g., $j = \text{LAD, LCX, RCA, etc.}$).
- *grafting angle* θ . Current clinical experience suggests that at least three possible termino-lateral (end-to-side) anastomoses are employed in clinical practice: antegrade (same direction for graft flow and native vessel flow in the anastomosis), T-shaped (graft perpendicular to the native vessel) and retrograde (opposite directions for graft flow and native vessel flow in the anastomosis). The virtual platform is employed to compare the hemodynamics in these different cases. The grafting angle is considered as geometrical parameter, in the range $\theta \in [25^\circ, 155^\circ]$, to deform the patient-specific configuration; antegrade

cases correspond to angles close to 45° , T-shaped to 90° , and retrograde to 135° , respectively.

We exploit the *centerlines-based parameterization* proposed in Ballarin et al. (2016) to deform the patient-specific mesh into a parametric one in an *automatic way* [i.e., without any new segmentation or remeshing, in contrast to what has been done, e.g., in Sankaran et al. (2012)]. This assumption is a necessary prerequisite for the efficient application of the reduced order model that needs to combine solutions representing different *geometrical configurations* still represented on the *same mesh*.

More in detail, the deformation of a single branch is carried out in three steps (see Fig. 4):

- (A) *Preprocessing* let $\gamma(s)$ be the centerline of the vessel, and $r(s)$ the radius of its maximum inscribed sphere. A moving coordinate frame $(t(s), n_1(s), n_2(s))$ attached to $\gamma(s)$ is computed by means of a parallel transport procedure (Bishop 1975). Three-dimensional vessels can then be represented using curvilinear cylindrical coordinates (ρ, φ, s) , corresponding to the local radius, angular coordinate and curvilinear abscissa, respectively.
- (B) *Curve deformation and radius variation*: let $\alpha \in [0, 0.9]$ be the severity of the stenosis and θ be the grafting angle. The reference radius $r(s)$ is locally decreased near the stenosis (located at $s = \hat{s}$) to obtain a parameterized radius $r(s; \alpha)$. We rotate the tangent vector $t(\bar{s})$ at the anastomosis (located at $s = \bar{s}$) of an angle θ , and apply a deformation to the reference curve $\gamma(s)$ to get a parameterized curve $\gamma(s; \theta)$.

Fig. 5 A centerline-based parameterization (anastomosis). Steps (A), (B) and (C) are performed to deform the green branch, and step (D) is performed for the anastomosis

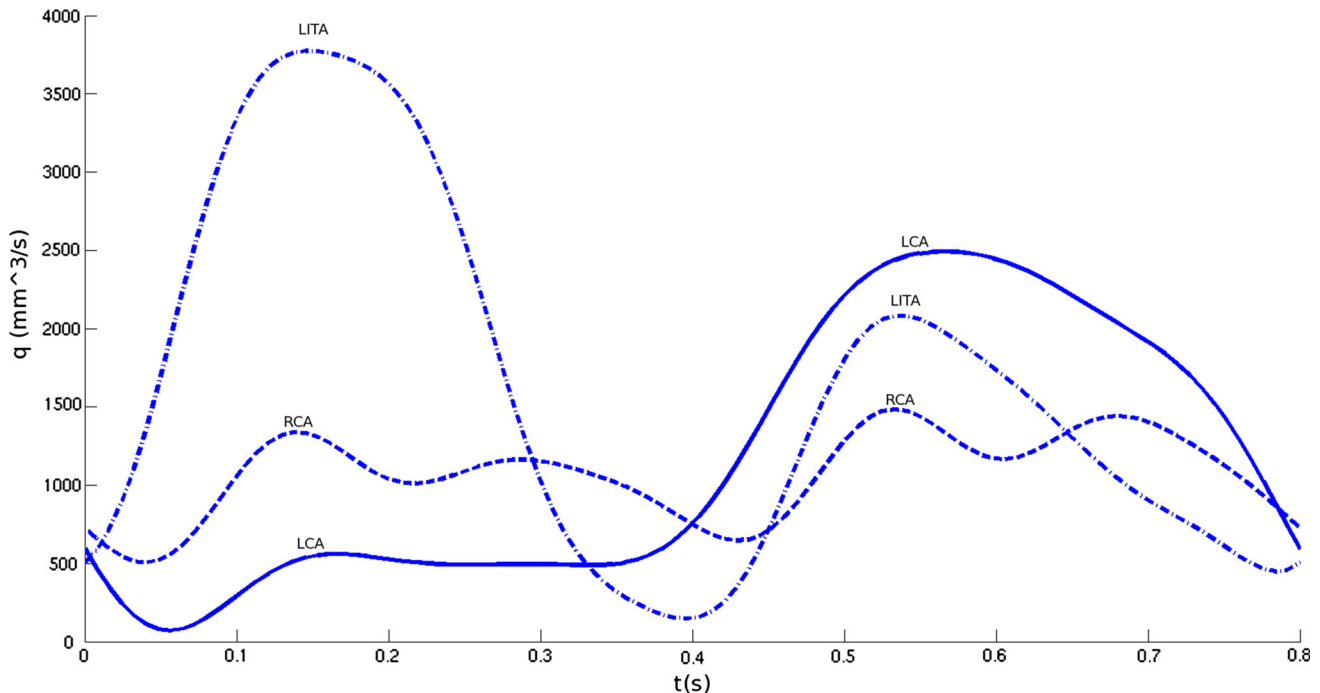
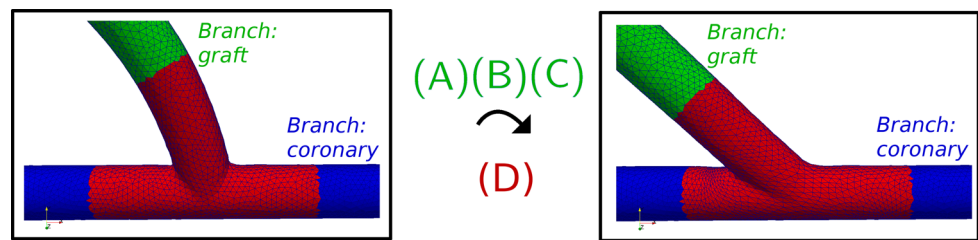


Fig. 6 Inlet flow rates q_i [LCA and RCA (Keegan et al. 2004), LITA (Ishida et al. 2001)]

(C) *Vessel deformation* we exploit the cylindrical vessel representation to obtain the deformed configuration of the branch, by computing the map $C(\cdot; \alpha, \theta) : \mathbb{R}^3 \rightarrow \mathbb{R}^3$,

$$C(x; \alpha, \theta) = \gamma(s(x); \theta) + \rho r(s(x); \alpha) [\cos \varphi(x) n_1(s(x); \theta) + \sin \varphi(x) n_2(s(x); \theta)].$$

The resulting map $C(\cdot; \alpha, \theta)$ allows to deform the three-dimensional vessel between the patient-specific branch (as reference configuration) and a deformed configuration, obtained as a function of the stenosis α and grafting angle θ (see the right blocks of Fig. 4).

These steps can be performed for each branch independently and then combined together to deform a network, as shown in Fig. 5 in the case of an anastomosis. Steps (A), (B) and (C) are performed to parameterize each vessel; then, an additional step (D) is carried out on each anastomosis to impose suitable interface conditions between adjacent

branches, ensuring the overall regularity of the deformation of the global geometry. Also this step is fully automatic, as shown in Ballarin et al. (2016).

2.2.2 Physical parameterization of flow rates

In addition to the geometrical parameterization discussed so far, we also consider a physical parameterization on flow rates at each inlet of the computational model (right coronary artery, left coronary artery, internal thoracic artery), because of its clinical relevance, e.g., when interested in the evaluation of the surgery under both rest or stress conditions. The parameterized flow rate is expressed as

$$q_i(t; f^i) = f^i \bar{q}_i(t), \quad i = \text{LCA, RCA, LITA}.$$

The parameter $f^i \in [2/3, 4/3]$ is a multiplicative factor on a reference flow rate $\bar{q}_i(t)$, adapted from Keegan et al. (2004) (LCA and RCA) and Ishida et al. (2001) (LITA). A plot is provided in Fig. 6 for the reference cases $f^i = 1$, corresponding to time-averaged Reynolds number equal to 100 (LCA

and RCA) and 130 (LITA). Note that LCA features dominant diastolic flow (i.e., coronary blood flow peaks in diastole), RCA is neither diastolic nor systolic dominant, while LITA is supposed to be systolic dominant.

2.3 POD–Galerkin reduced order models for parameterized blood flows

In this section we summarize the ROM employed in our numerical simulations. The hemodynamics in the CABG configuration is supposed to be modelled by unsteady parameterized Navier–Stokes equations, under rigid walls assumptions and constant viscosity ν : find velocity \mathbf{u} and pressure p such that

$$\begin{cases} \frac{\partial}{\partial t} \mathbf{u} - \nu \Delta \mathbf{u} + (\mathbf{u} \cdot \nabla) \mathbf{u} + \nabla p = 0 & \text{in } \Omega_o(\mu_g) \times (0, T), \\ \operatorname{div} \mathbf{u} = 0 & \text{in } \Omega_o(\mu_g) \times (0, T), \\ \mathbf{u} = g_D(\mu_p) & \text{on } \Gamma_D \times (0, T), \\ \mathbf{u} = 0, & \text{on } \Gamma_{o,W}(\mu_g) \times (0, T), \\ \nu \frac{\partial \mathbf{u}}{\partial n} - pn = 0, & \text{on } \Gamma_N \times (0, T), \\ \mathbf{u}|_{t=0} = g_0(\mu_p), & \text{in } \Omega_o(\mu_g). \end{cases}$$

The parameters are denoted by $\mu = (\mu_p, \mu_g) \in \mathcal{D} \subset \mathbb{R}^{P+G}$, including both physical parameterization on the boundary conditions $\mu_p = (f^{LCA}, f^{RCA}, f^{LITA})$ and geometrical parameters $\mu_g = (\alpha, \theta)$, introduced in Sects. 2.2.2 and 2.2.1, respectively. Thanks to the parameterization of the domain, the patient-specific configuration Ω is mapped into a parameterized one $\Omega_o(\mu_g)$, along with its lateral boundary $\Gamma_{o,W}(\mu_g)$. Inlet sections Γ_D and outlet sections Γ_N are fixed, and the initial condition g_0 is the solution of the corresponding steady-state problem. Homogeneous Neumann boundary conditions are imposed on outlet sections.

A FE approximation for spatial discretization and an implicit Euler scheme for time discretization are chosen as the high-fidelity method, over which our proposed reduced order model is built. Let us denote by V_h and Q_h two finite-dimensional spaces for velocity and pressure, of dimension $N_{\mathbf{u}}^h$ and N_p^h , respectively, based on a FE discretization of the patient-specific geometry of mesh size h . The nonlinear system resulting from a FE discretization in space and implicit Euler discretization in time of the Navier–Stokes equations is: given $\mu \in \mathcal{D}$ and $(\mathbf{u}(t^n), \mathbf{p}(t^n))$, find $(\mathbf{u}(t^{n+1}), \mathbf{p}(t^{n+1}))$ such that

$$\begin{bmatrix} \frac{M(\mu)}{\Delta t} + \nu A(\mu) + C(\mathbf{u}(t^{n+1}; \mu); \mu) & B^T(\mu) \\ B(t^{n+1}; \mu) & 0 \end{bmatrix} \begin{bmatrix} \mathbf{u}(t^{n+1}; \mu) \\ \mathbf{p}(t^{n+1}; \mu) \end{bmatrix} = \begin{bmatrix} \frac{M(\mu)}{\Delta t} \mathbf{u}(t^n; \mu) + \mathbf{f}(t^{n+1}) \\ \mathbf{0} \end{bmatrix} \quad (1)$$

for each time step $n = 0, \dots, T/\Delta t - 1$, where $\mathbf{u}(0)$ is the discrete counterpart of the initial condition, and the right-hand side term $\mathbf{f}(t)$ encodes non-homogeneous Dirichlet boundary conditions through a lifting function. The parameterized tensors M, A, B and C are, respectively, the mass, stiffness, incompressibility and advection terms of the parameterized Navier–Stokes equations.

The proposed reduced order model is able to provide large computational speedups thanks to the separation between an offline stage (computationally expensive, but done only once) and an online stage (computationally inexpensive, carried out for each virtual scenario of interest). During the offline stage a set $\mathcal{E}_{\text{train}} = \{\mu^1, \dots, \mu^{N_{\text{train}}}\} \subset \mathcal{D}$ of N_{train} points, chosen randomly over the parameter space \mathcal{D} , is defined. For each $\mu \in \mathcal{E}_{\text{train}}$ problem (1) is solved for $n = 0, \dots, T/\Delta t - 1$, and all the corresponding solutions (both velocity and pressure) are saved. A proper orthogonal decomposition (POD) (Berkooz et al. 1993; Ravindran 2000) is performed to select the few most relevant velocity (pressure, respectively) basis functions, stored in matrices $Z_{\mathbf{u}}$ (Z_p , resp.) and which span the reduced basis spaces V_N and Q_N of (small) dimension $N_{\mathbf{u}}$ and N_p . Therefore, in the online stage, a Galerkin projection on (V_N, Q_N) is carried out, and the resulting problems reads: for any $\mu \in \mathcal{D}$, given $\mathbf{u}_N(t^n; \mu)$, solve

$$\begin{bmatrix} \frac{M_N(\mu)}{\Delta t} + \nu A_N(\mu) + C_N(\mathbf{u}_N(t^{n+1}; \mu); \mu) & B_N^T(\mu) \\ B_N(\mu) & 0 \end{bmatrix} \begin{bmatrix} \mathbf{u}_N(t^{n+1}; \mu) \\ \mathbf{p}_N(t^{n+1}; \mu) \end{bmatrix} = \begin{bmatrix} \frac{M_N(\mu)}{\Delta t} \mathbf{u}_N(t^n; \mu) + \mathbf{f}_N(t^{n+1}) \\ \mathbf{0} \end{bmatrix},$$

for any $n = 0, \dots, T/\Delta t - 1$, where, e.g., $A_N(\mu) = Z_{\mathbf{u}}^T A(\mu) Z_{\mathbf{u}}$ is now a matrix of dimension $N_{\mathbf{u}} \ll N_{\mathbf{u}}^h$. We refer to Ballarin et al. (2016) and Ballarin et al. (2015) for additional details on the analysis of this reduced order model such as the comparison between high fidelity and reduced order solutions, as well as Manzoni (2014), Rozza et al. (2013) and Burkardt et al. (2006) for related reduction methods.

3 Numerical results

For each patient in the dataset we report in Table 2 the number of considered physical and geometrical parameters, discretization of the high-fidelity FE approximation, and CPU times of both high fidelity and reduced order problems. A Taylor-Hood $\mathbb{P}_2 - \mathbb{P}_1$ discretization is employed for the high-fidelity FE discretization; 80 steps per cardiac cycle (of period 0.8 s), for 2 cardiac cycles, are simulated. We will further discuss the performance of the proposed reduced order framework in the next section.

Relevant computational indices are obtained in a post-processing stage after the reduced order simulation in order

Table 2 Details of the reduced order model. FE computations are carried out on 32 processors on modern HPC clusters, and the reported CPU time is the product of the wall time and the number of processors. ROM computations are performed, instead, in serial

<i>Patient</i>	A	B	C	D	E
Num. physical parameters	3	0	2	2	0
LCA inlet flow rate parameters	1	No	1	1	No
RCA inlet flow rate parameters	1	No	No	No	No
LITA inlet flow rate parameters	1	No	1	1	No
Num. geometrical parameters	3	3	2	2	3
LCA parameterized stenosis	No	No	No	No	No
LAD/Diag parameterized stenosis	1	1	2	2	1
LCX/OM parameterized stenosis	1	No	No	No	No
RCA parameterized stenosis	1	1	No	No	1
Parameterized anastomosis	No	1	No	No	1
Total number of FE dofs	1 325 530	1 826 495	813 197	1 325 044	2 038 891
FE CPU time/cardiac cycle	400–450 h	450–500 h	200–250 h	400–450 h	500–550 h
ROM CPU time/cardiac cycle	5–15 min	25–35 min	5–15 min	5–15 min	25–35 min
<i>Patient</i>	F	G	H	I	J
Num. physical parameters	2	2	2	3	0
LCA inlet flow rate parameters	1	1	1	1	No
RCA inlet flow rate parameters	No	No	No	1	No
LITA inlet flow rate parameters	1	1	1	1	No
Num. geometrical parameters	3	0	2	4	2
LCA parameterized stenosis	1	No	No	No	No
LAD/Diag parameterized stenosis	1	No	2	2	1
LCX/OM parameterized stenosis	1	No	No	1	No
RCA parameterized stenosis	No	No	No	1	No
Parameterized anastomosis	No	No	No	No	1
Total number of FE dofs	970 618	1 261 527	1 624 370	1 426 060	1 219 918
FE CPU time/cardiac cycle	350–400 h	350–400 h	400–450 h	350–400 h	400–450 h
ROM CPU time/cardiac cycle	5–15 min	5–15 min	5–15 min	5–15 min	25–35 min

to compare the flow patterns for different values of the parameters. In particular, we analyze wall shear stress (WSS), oscillatory shear index (OSI), transversal velocity profiles, and pressure drops, because of their relation to the process of intimal thickening (Loth et al. 2008):

- the existence of a safe bandwidth of wall shear stress (defined as $\mathbf{t} - \mathbf{t} \cdot \mathbf{n} \mathbf{n}$, being \mathbf{t} the traction acting on the lateral wall of outer normal \mathbf{n}) has been suggested in Kleinstreuer et al. (1991), highlighting that both low and high WSS may favor the restenosis process. In fact, high WSS may lead to endothelial injury and cause the development of a lesion. Instead, low WSS and long particle residence time in flow recirculation zones favors the deposit of fatty materials and cholesterol on the surface of the lumen, causing the growth of the atheroma. Results are presented either as instantaneous WSS values (usually at systole or diastole) or time-averaged WSS, denoted by

TAWSS, obtained as the average of WSS over a cardiac cycle (0, T)

$$\text{TAWSS} = \frac{1}{T} \int_0^T |\mathbf{WSS}(t)| dt;$$

- a correlation between plaque location and oscillating shear stress has been described in Ku et al. (1985), showing that oscillations in the direction of wall shear may cause atherogenesis. To assess the oscillatory nature of WSS we employ the OSI, defined as

$$\text{OSI} = \frac{1}{2} \left[1 - \frac{\left| \int_0^T \mathbf{WSS}(t) dt \right|}{\int_0^T |\mathbf{WSS}(t)| dt} \right] \quad 0 \leq \text{OSI} \leq 0.5;$$

- the formation of Dean vortices in the region distal to the anastomosis is detected thanks to transversal velocity

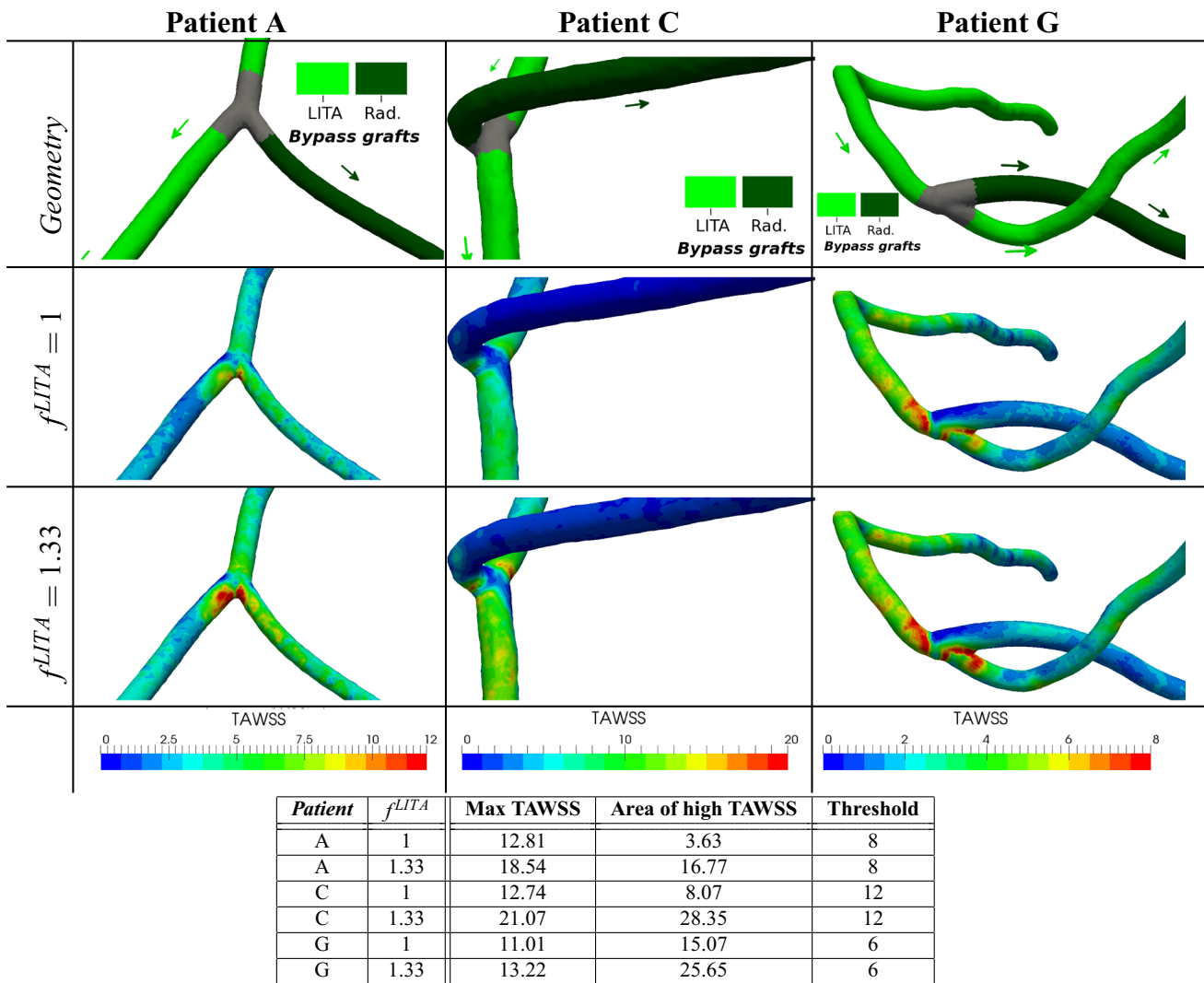


Fig. 7 Virtual scenario I, Y-graft between LITA and radial artery: comparison of TAWSS (Pa) for different inflow boundary conditions. The table reports the maximum TAWSS (Max TAWSS) and the area, computed in mm², of the vessel characterized by high values of TAWSS

(area of high TAWSS); the threshold (Threshold) used to identify high values of TAWSS has been chosen at approximately 2/3 of the range shown in the 3D plot

profiles. In fact, secondary flow structures (i.e., perpendicular to the flow direction) are usually not negligible at the anastomosis, and the formation of a pair of vortical structures has been observed (Sherwin and Doorly 2003).

Regions of interest are the *heel* and *toe* of the graft, and the proximal and distal *arterial floor* near the anastomosis (see also Fig. 1) (Staalsen et al. 1995; Loth et al. 2008). We refer to heel of the graft as the location of the proximal suture line, while the toe of the graft refers to the distal suture line. The adjectives *proximal* and *distal* are defined with respect to the direction of the flow in the native coronary artery.

We report these computational indices for different values of the parameters on several cases of the available patient-specific dataset. To provide an easier comparison, only one or two parameters are varied at a time in the

graphical visualization; the remaining parameters are set to a standard default value, chosen equal to one for flow rates factors (standard flow rate), critical values of stenosis (90%), undeformed anastomosis configuration (no variation of the grafting angle with respect to the patient-specific one). However, the reduced order methodology is capable of varying more the one parameter at a time.

We collect the results as follows, in order to discuss each scenario separately in the next section:

- I. *virtual scenario I* concerns the effect of flow rate variation in Y-grafts. Several Y-graft configurations are compared through the computation of TAWSS near the Y-graft. Both Y-graft between LITA and radial artery (Fig. 7) and Y-graft between LITA and SVG (Fig. 8) are considered. Two different inflow boundary conditions

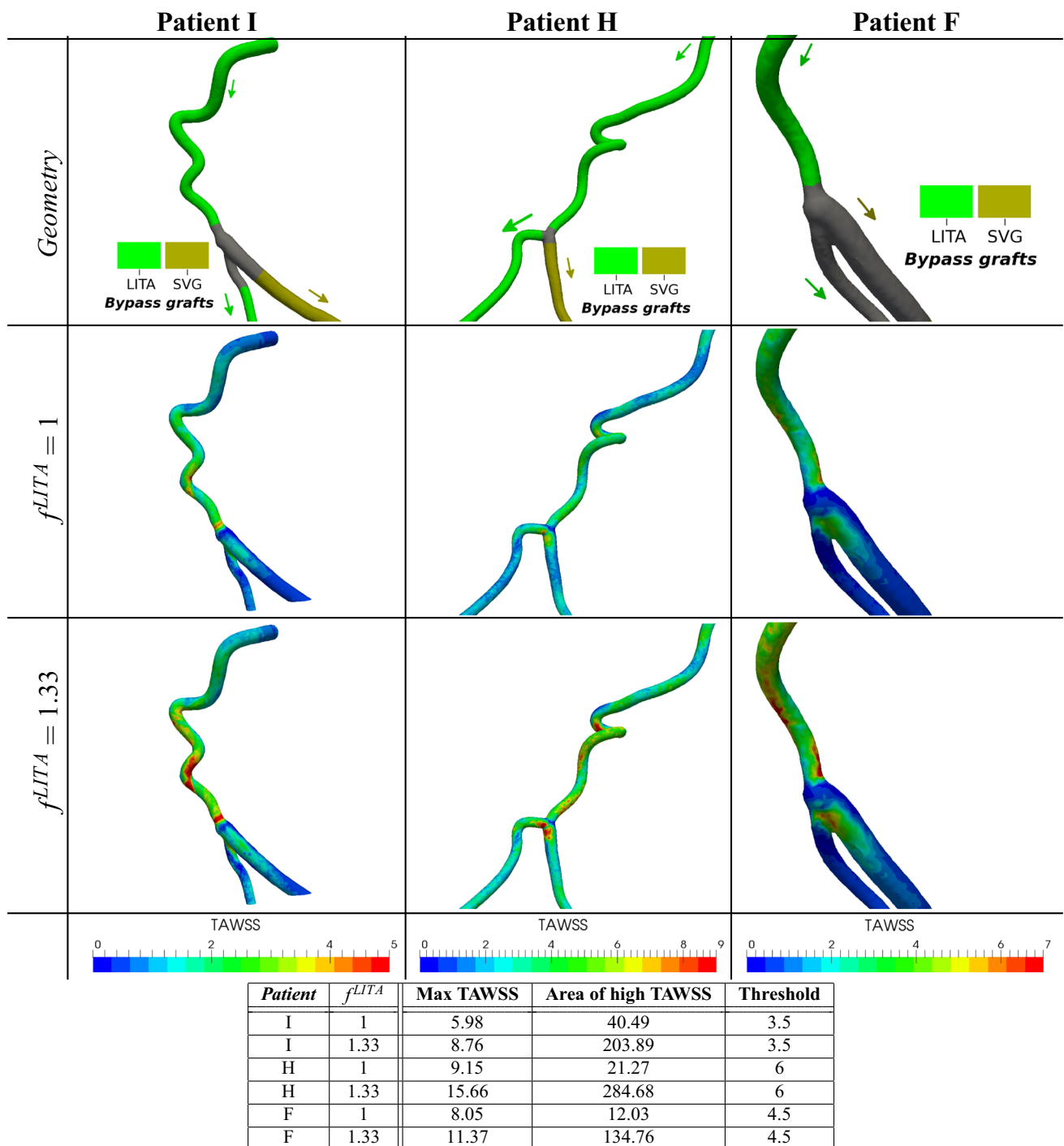


Fig. 8 Virtual scenario I, Y-graft between LITA and SVG: comparison of TAWSS (Pa) for different inflow boundary conditions. The table reports the maximum TAWSS (Max TAWSS) and the area, computed in mm², of the vessel characterized by high values of TAWSS (area of

high TAWSS); the threshold (Threshold) used to identify high values of TAWSS has been chosen at approximately 2/3 of the range shown in the 3D plot

are studied, corresponding to standard graft flow rate ($f^{LITA} = 1$) and increased graft flow rate ($f^{LITA} = 1.33$).

II. *virtual scenario II* focuses on the effect of flow rate variation in sequential grafts. Several sequential grafts

are compared through the computation of the TAWSS near the side-to-side anastomosis. A cross-anastomosis of a graft employed distally for the revascularization of the right coronary tree is considered in Patient A of Fig. 9, while antegrade anastomoses for the revas-

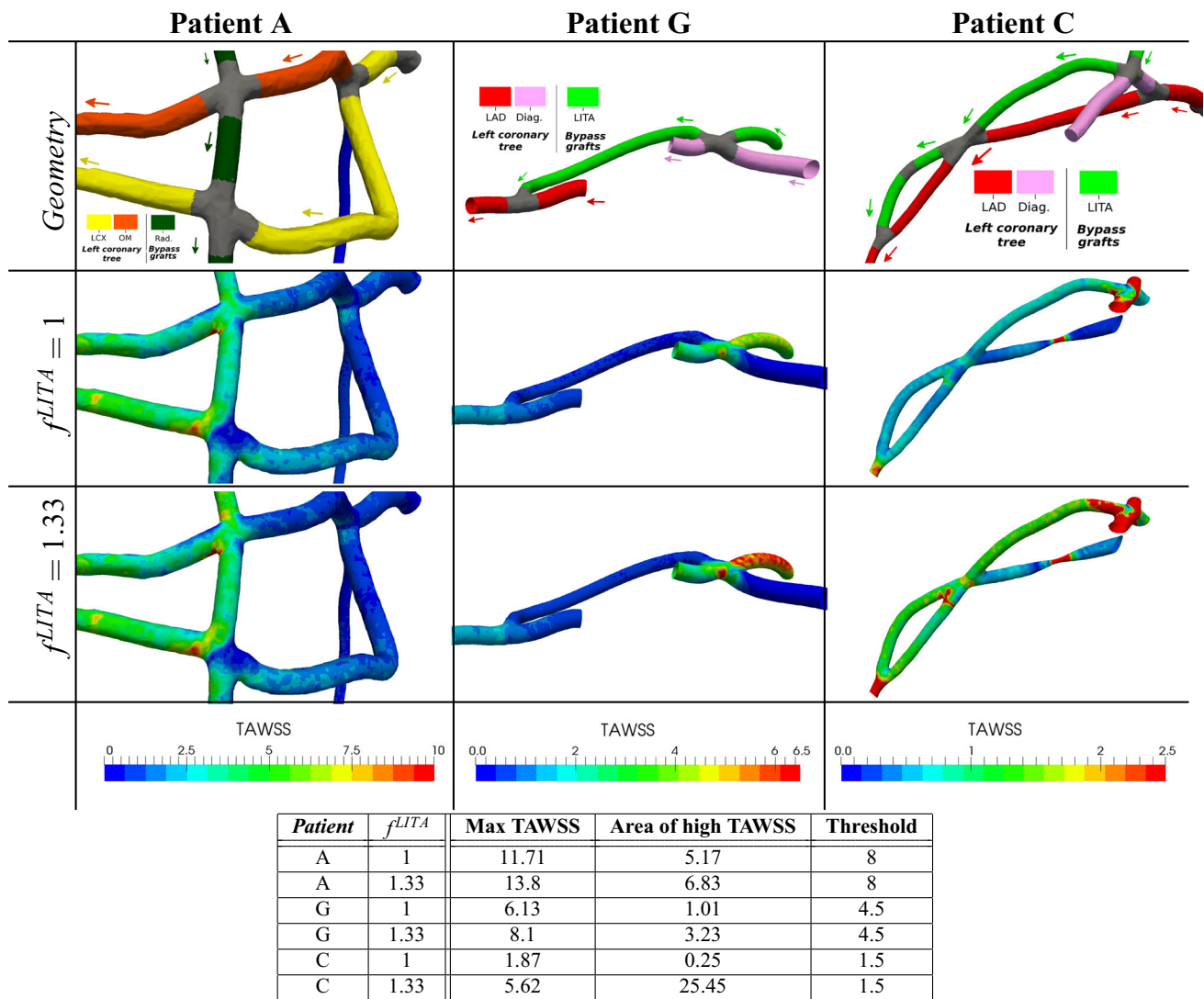


Fig. 9 Virtual scenario II, sequential grafts: comparison of TAWSS (Pa) for different inflow boundary conditions and stenosis. The table reports the maximum TAWSS (Max TAWSS) and the area, computed in mm², of the vessel characterized by high values of TAWSS (area of

high TAWSS); the threshold (Threshold) used to identify high values of TAWSS has been chosen at approximately 2/3 of the range shown in the 3D plot

cularization of the left coronary tree are considered in Patients C and G of Fig. 9. Also in this case, different boundary conditions are studied, corresponding to standard graft flow rate ($f^{LITA} = 1$) or increased graft flow rate ($f^{LITA} = 1.33$).

III. *virtual scenario III* is about the effect of flow rate and stenosis variation on anastomosis. As a first case, we compare surgery outcomes for different stenosis severity on the left coronary tree, by means of OSI and WSS (Figs. 10, 11). This pathology is usually surgically treated by LITA grafts. As a second case, we compare computational indices for different stenosis severity on the right coronary tree, considering in particular a case where a radial graft is employed (Fig. 12)

IV. *virtual scenario IV* concerns anastomosis geometrical variation. Also in this scenario we consider both left and right coronary trees, and different grafting types. Figures 13, 14 and 15 show the results on WSS, transversal velocity profiles and pressure drop for a LITA-LAD anastomosis (arterial graft) in the left coronary tree. Figure 16 details instead the numerical results on WSS on a SVG-PDA anastomosis (venous graft) in the right coronary tree.

V. finally, *virtual scenario V* studies the effect of flow rate and stenosis variation on native coronary bifurcations, especially on the left coronary tree. Results on TAWSS are provided in Figs. 17, 18 and 19 for three different patients. Moreover, thanks to our virtual framework it is

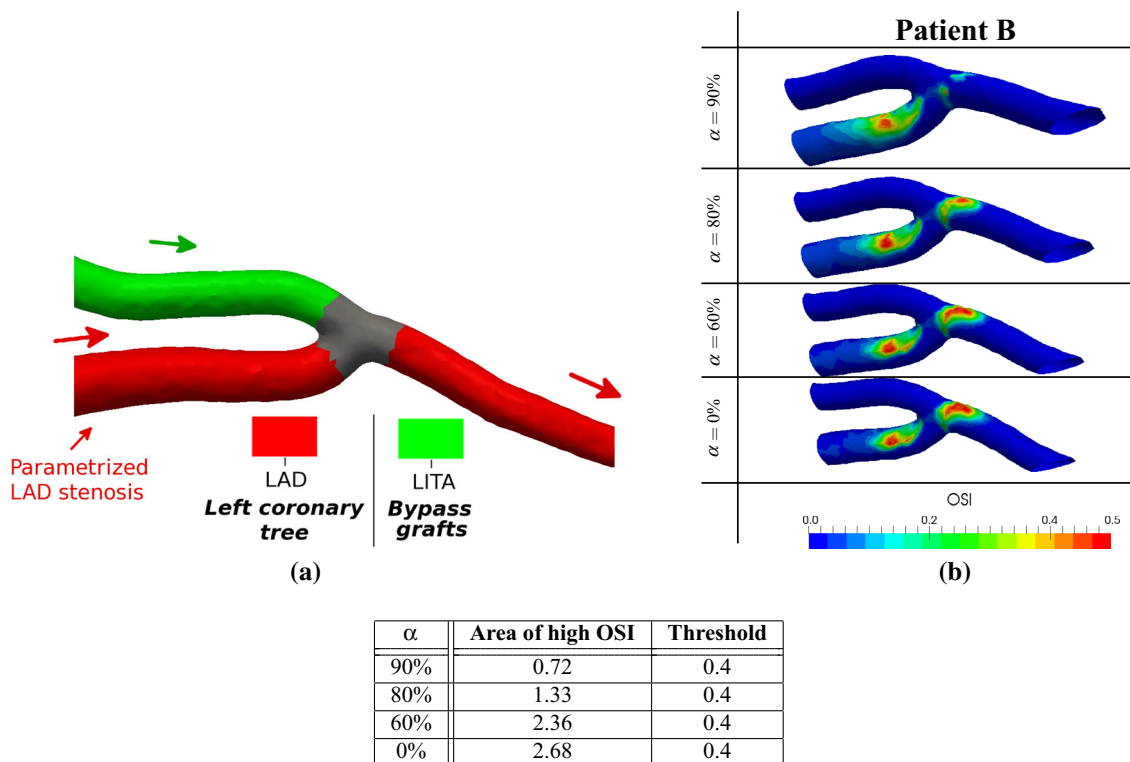


Fig. 10 Virtual scenario III, LITA to LAD anastomosis: comparison of OSI for decreasing proximal stenosis. The table reports the area, computed in mm^2 , of the vessel characterized by high values of OSI (area of high OSI); the threshold (Threshold) used to identify high values of OSI has been chosen equal to 0.4.

possible to virtually remove the bypass graft and compare the hemodynamics before and after the surgery. A proof of concept of this scenario is provided in Fig. 20.

4 Discussion

4.1 State of the art on parameterized problems and novelties of the proposed virtual surgery platform

Early numerical results on three-dimensional idealized end-to-side anastomoses have been proposed in Fei et al. (1994), Inzoli et al. (1996), Kute and Vorp (2001) and Sherwin et al. (1999), under the assumption of steady flow conditions, and in Bertolotti and Deplano (2000), Bertolotti et al. (2001), Deplano et al. (2001), Lei et al. (2000) and Ross Ethier et al. (1998) for time-dependent flow profiles. Since these early attempts, *parametric studies* have attracted considerable attention (Pagni et al. 1997; Sabik and Blackstone 2008; Sabik et al. 2003; Nordgaard et al. 2010; Swillens et al. 2012; Kute and Vorp 2001; Keynton et al. 1991). Among these, variation of *inlet boundary conditions* allows us to account for different exercise conditions of the patient (e.g., stress conditions vs rest conditions). Moreover, variation of graft flow rate is observed in the clinical practice

in the internal thoracic artery (Pagni et al. 1997; Sabik and Blackstone 2008; Sabik et al. 2003); this results in increased graft flow rate for increased native stenosis degree. Independent variation of graft flow rate is therefore another aspect of remarkable clinical interest. Numerical simulations to take this aspect into account have been performed on idealized configurations (Kute and Vorp 2001; Keynton et al. 1991), and in Nordgaard et al. (2010) and Swillens et al. (2012) on a porcine model. A parameterization of inlet boundary conditions is applied also in our work and integrated into a model reduction framework by means to be applied on multiplicative factors on inlet flow rates. The blood is assumed to be a Newtonian fluid in this work, as in most of the existing literature summarized by several review papers (Ghista and Kabinejadian 2013; Migliavacca and Dubini 2005; Owida et al. 2012) and recent publications (Ramachandra et al. 2016; Sankaran et al. 2016; Tran et al. 2017; Zhang et al. 2016, 2015). However, as discussed in Chen et al. (2006) and Gijssen et al. (1999), non-Newtonian effect may be captured employing a Newtonian model at a rescaled Reynolds number. Even though a detailed comparison of Newtonian and non-Newtonian constitutive models is out of the scope of this work, we highlight that another possible application of interest for the proposed parameterized model is its capability to mimic

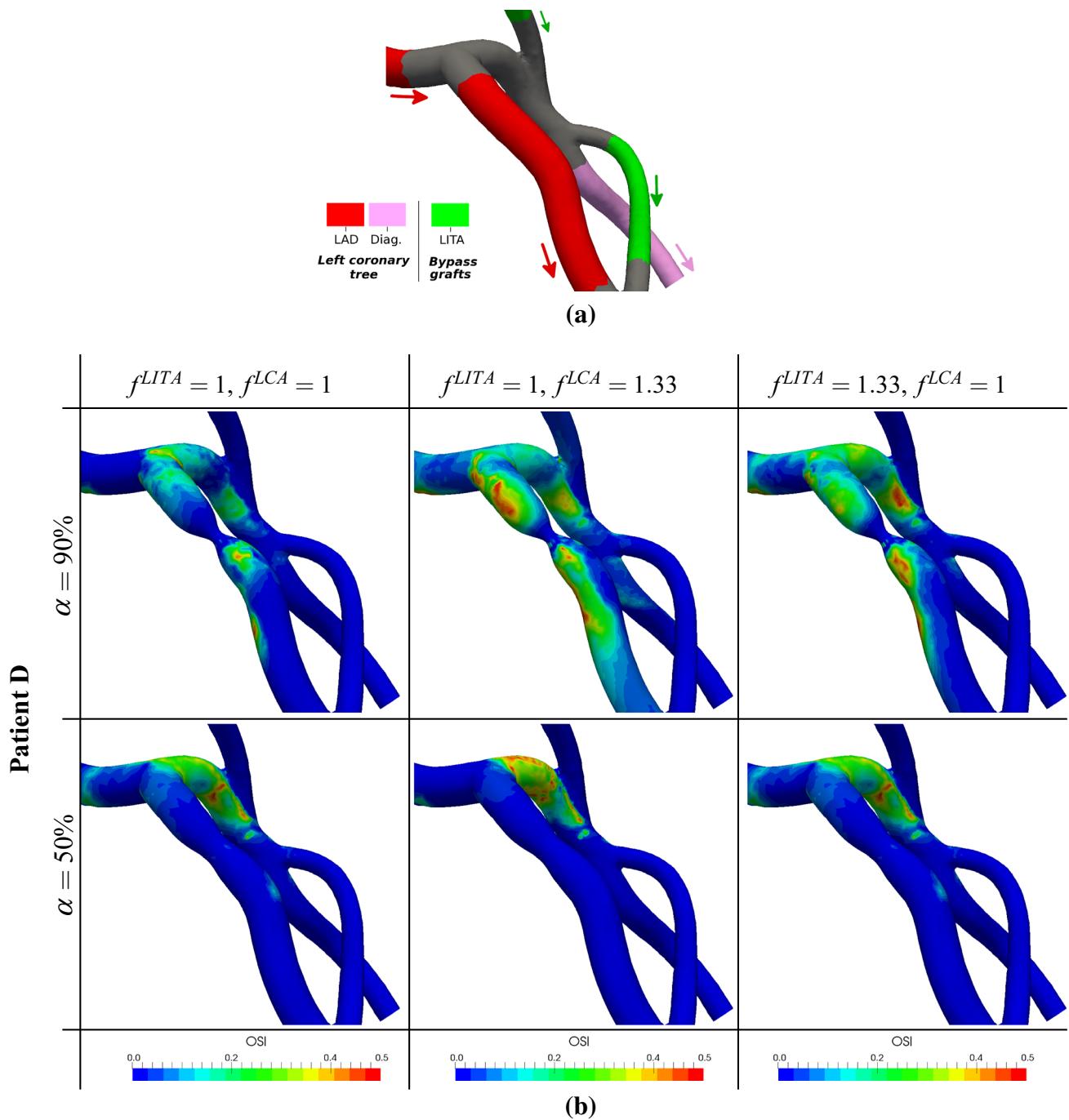


Fig. 11 *Virtual scenario III*, LITA to diag anastomosis, in a sequential graft: comparison of OSI for different inflow boundary conditions and stenosis. Coronary arteries and bypass grafts near the studied anastomosis. *Colored arrows* denote blood flow direction

non-Newtonian effects thanks to a rescaled Reynolds number.

Large attention has also been paid to *local geometrical variations of CABGs* (Lei et al. 1997; Dur et al. 2011; Marsden et al. 2008; Probst et al. 2010; Sankaran and Marsden 2010; Politis et al. 2008; Kabinejadian and Ghista 2012; Kabinejadian et al. 2010; Wen et al. 2011), in order to propose new design or optimize existing ones performing variation of

grafting angles (Fei et al. 1994; Sherwin and Doorly 2003; Giordana et al. 2005; Keynton et al. 1991; Staalsen et al. 1995; Jackson et al. 2001; Freshwater et al. 2006; Do et al. 2011) or graft-to-host diameter ratio (Bonert et al. 2002; Qiao and Liu 2006; Idu et al. 1999; Towne et al. 1991; Xiong and Chong 2008). The proposed virtual surgery platform can address grafting angles variations in an automatic way (without remeshing). To the best of our knowledge this

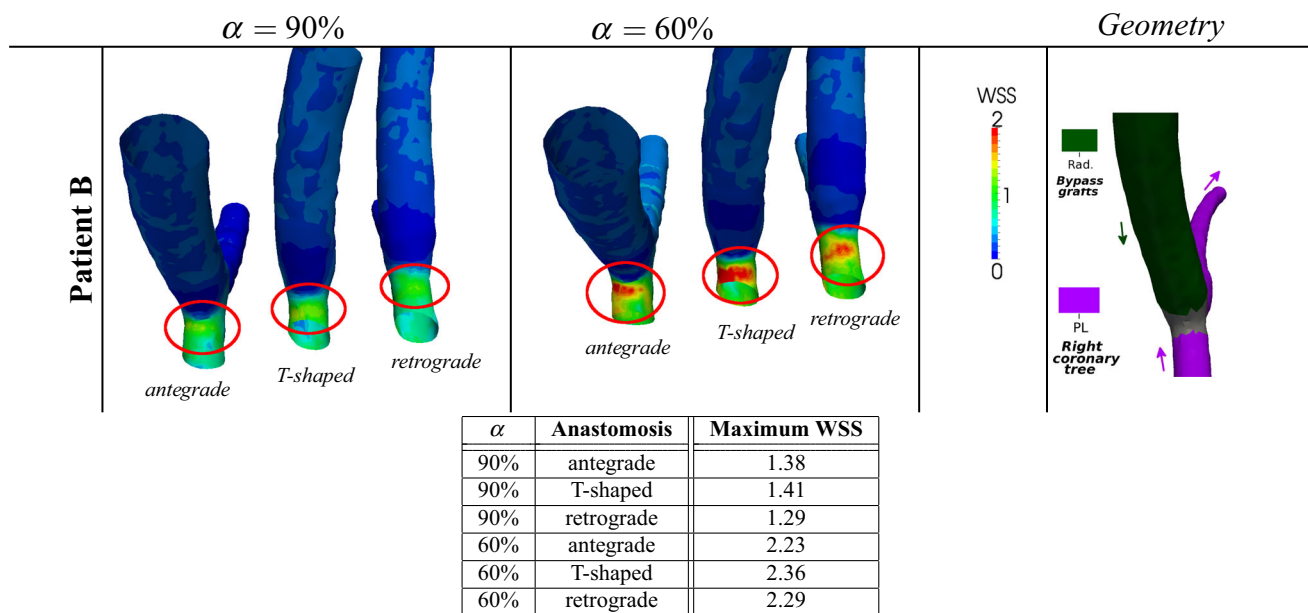


Fig. 12 Virtual scenario III, radial to PL anastomosis: comparison of WSS (Pa) for three anastomoses types

is the first study for which such an automatic procedure is applied to CABGs. Diameter ratio variation is not taken into account by the current framework. The motivation is that grafts employed in the clinical practice come from autologous materials and thus their diameter cannot be easily varied in the clinical practice, especially considering several practical constraints in case of extensive coronary artery disease. It is thus far more important to consider a complete patient-specific network and optimize it, rather than optimize representative but idealized configurations.

Therefore, another significant feature of the present approach is the capability to carry out parametric studies on *patient-specific* CABGs. Few studies have been carried out on patient-specific configurations, reconstructed from clinical data. Among them we mention (Boutsianis et al. 2004; Chaichana et al. 2011; Kim et al. 2010; Tran et al. 2017; Zhang et al. 2008, 2016, 2015) on native (healthy) coronary arteries, and (Frauenfelder et al. 2007; Dur et al. 2011; Sankaran et al. 2012; Guerciotti et al. 2016; Ramachandra et al. 2016; Sankaran et al. 2016) on coronary artery bypass grafts. Our current dataset is, however, larger, and more complete (with respect to anastomosis features, grafting procedures, coronary artery disease) than those in previous references. In particular, (Frauenfelder et al. 2007) proposed CFD simulations only on two patients, the first one featuring a single graft and the second one a double sequential grafts. Both surgeries, however, were performed only with saphenous vein grafts, and more complex structures (such as Y-grafts) were not studied. Geometrical variations were considered instead in Dur et al. (2011), but they were performed on two-dimensional configurations and then applied to the three-dimensional patient-specific configuration in a post-

processing stage. Moreover, the variation of grafting angles proposed in Sankaran et al. (2012) requires a new segmentation for each new angle, as well as the variation of stenosis in Guerciotti et al. (2016) requires a remeshing. Both are time consuming procedures that do not take advantage of the parameterized formulation. Instead, in this work we propose an automatic geometrical variation capable of exploiting the parameterization of the problem.

Overall, the most significant contribution of the proposed virtual surgery platform is to combine all these aspects into a *reduced order modeling framework*, capable of automatically handling physical and geometrical parameters, to numerically obtain quantities of interest in (as we will detail in the next section) a very fast way, reducing days of CPU time on a cluster to few minutes on a laptop. This is possible thanks to a specialized shape parameterization map, tailored for CABG networks, and projection-based ROM based on a POD–Galerkin approach for unsteady Navier–Stokes equations.

4.2 Computational performance of the virtual surgery platform

Details of the virtual surgery platform are provided in Table 2. The high-fidelity discretization is queried only during the offline stage (see Sect. 2.3); instead, the online reduced model is used for each query to the virtual surgery platform. The total number of degrees of freedom for the high-fidelity simulation is of order 10^6 , while a considerably smaller number of degrees of freedom, corresponding to 150 reduced basis functions (accounting for both velocity and pressure approximation) are required in the reduced order model. These

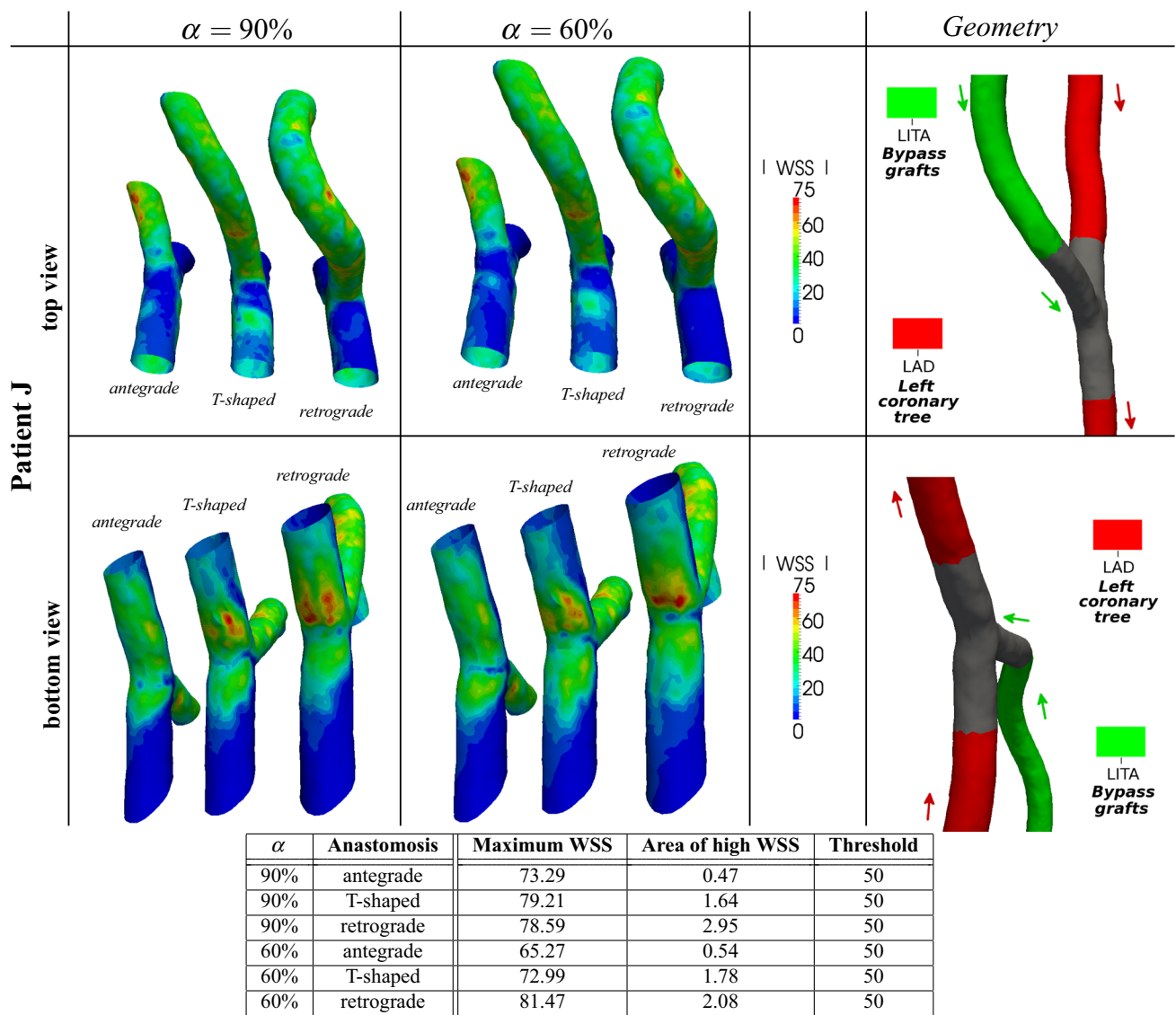


Fig. 13 Virtual scenario IV, LITA to LAD anastomosis: comparison of WSS (Pa) at peak systole for three anastomosis types. The table reports the maximum WSS (Max WSS) and the area, computed in mm², of

the vessel characterized by high values of WSS (area of high WSS); the threshold (Threshold) used to identify high values of WSS has been chosen at approximately 2/3 of the range shown in the 3D plot

reduced basis functions account for 99% of the information retained in the snapshots on $\mathcal{E}_{\text{train}}$, selected during the offline stage.

The considerable reduction of degrees of freedom entails large computational savings in the proposed reduced order framework. In fact, high-fidelity simulations are performed in parallel, on 32 processors, and require approximately 10 wall time hours per cardiac cycle¹. Reduced order simulations, instead, are performed on a single processor and require

only CPU times of the order of minutes, with computational savings in terms of wall time up to 99%. Thus, the main advantage of the proposed reduced order approach is its capability to compare several different physical or geometrical configurations in computational times considerably smaller than ones obtained by standard finite element simulations, still preserving the same degree of accuracy.

A comparison of the proposed reduced order model to the high-fidelity discretization is shown in Fig. 21 for a representative case (virtual scenario IV, Patient J, variation of the anastomosis) in our dataset. Three different values of the grafting angle θ are chosen, corresponding to antegrade ($\theta = 45^\circ$), T-shaped ($\theta = 90^\circ$) and retrograde ($\theta = 135^\circ$) anastomosis. For each choice of θ , high-fidelity computations

¹ The number of wall time hours needs to be multiplied by the number of processors to obtain the actual CPU time spent on the cluster. The actual CPU time is listed in Table 2 in order to have a fair comparison between the high-fidelity model (which runs in parallel on several processors) and ROM (which runs in serial).

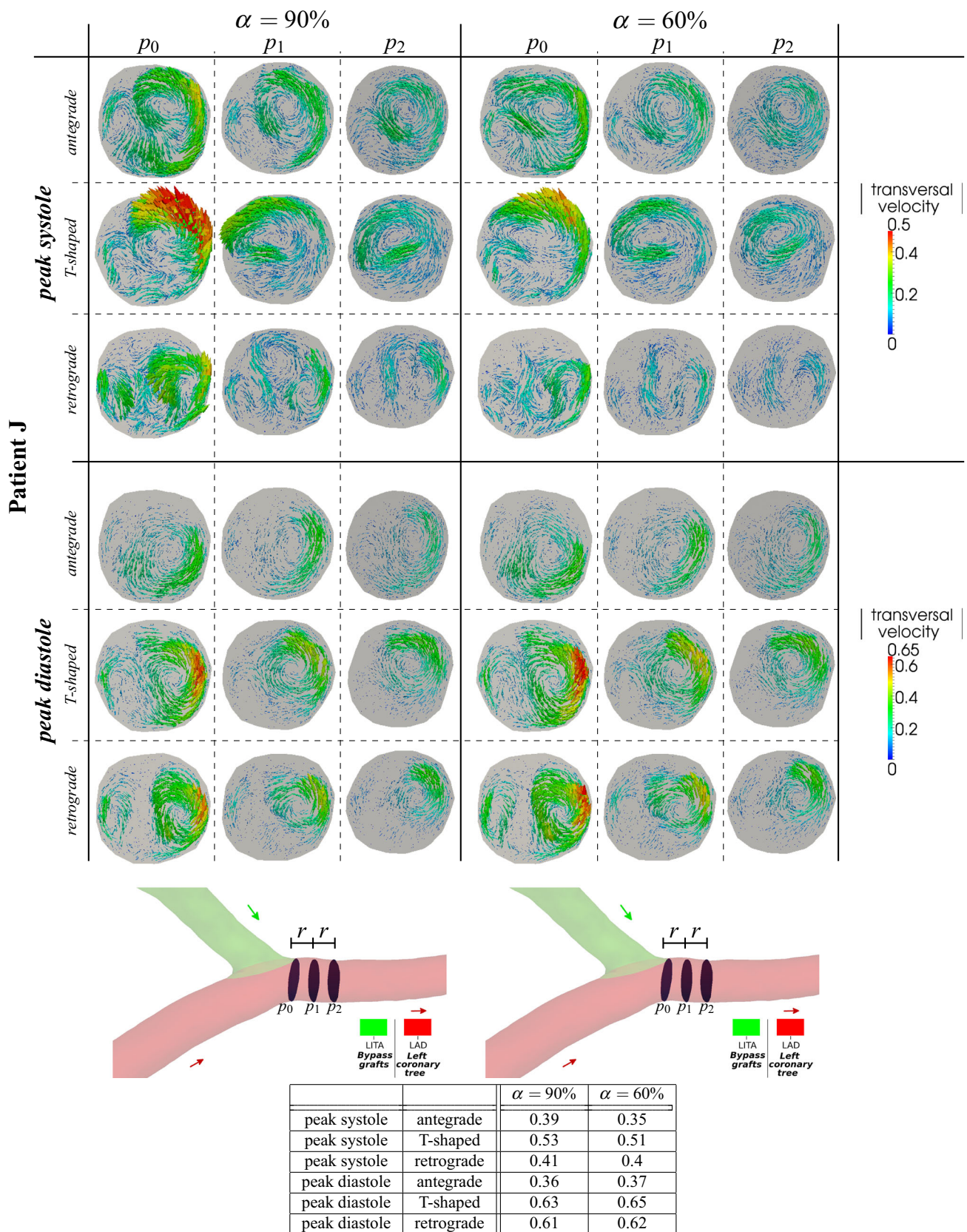


Fig. 14 Virtual scenario IV, LITA to LAD anastomosis: comparison of normalized transversal velocity profiles at different phases of the cardiac cycle for three anastomoses types. The table reports the maximum value of normalized transversal velocity

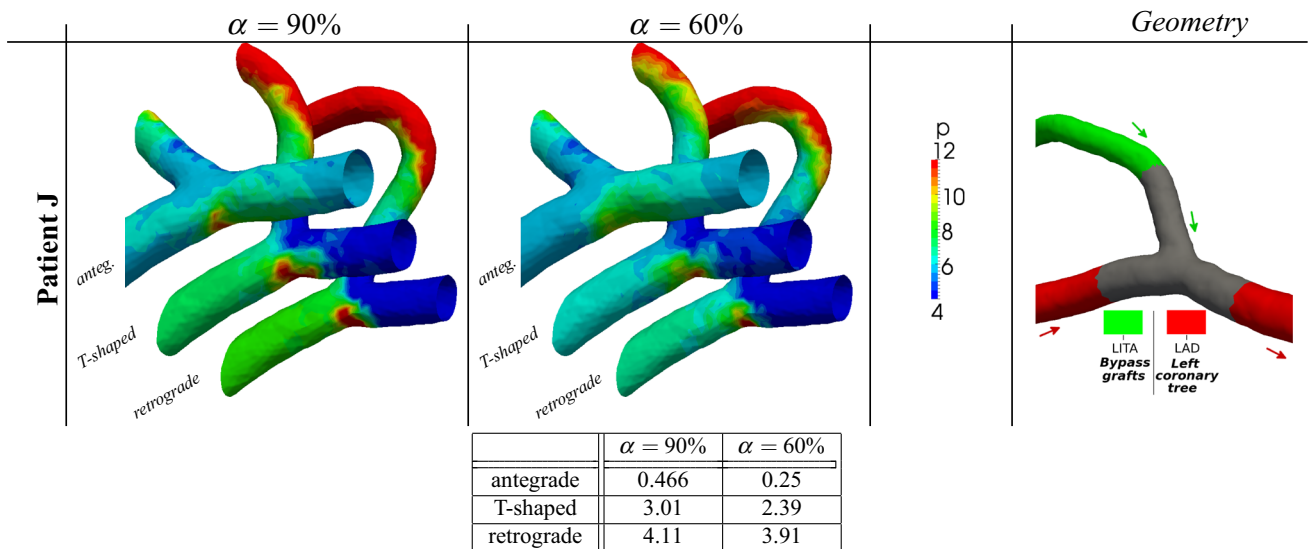


Fig. 15 Virtual scenario IV, LITA to LAD anastomosis: comparison of pressure drop (mmHg) at peak systole for three anastomoses types. The table reports the value of pressure drop in the anastomosis

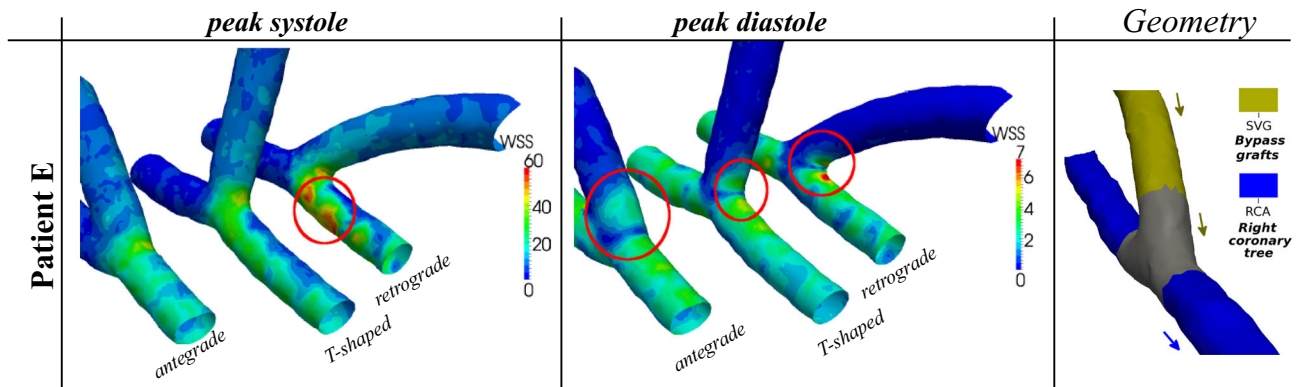


Fig. 16 Virtual scenario IV, SVG to PDA anastomosis: comparison of WSS (Pa) at different phases of the cardiac cycle for three anastomoses types

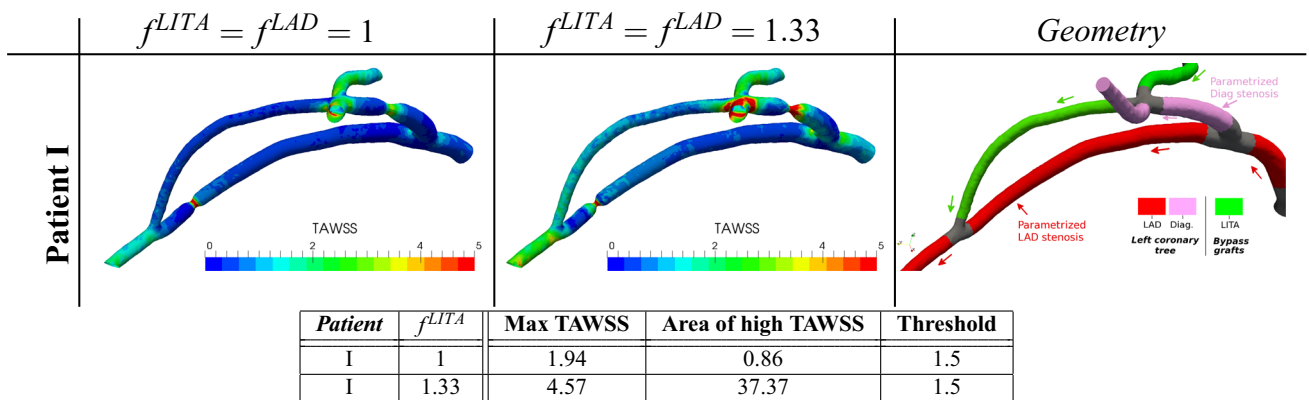


Fig. 17 Virtual scenario V, LITA-Diag-LAD sequential graft: comparison of TAWSS for different inflow boundary conditions and stenosis. The table reports the maximum TAWSS (max TAWSS) and the area, computed in mm^2 , of the vessel characterized by high values of TAWSS

(area of high TAWSS); the threshold (Threshold) used to identify high values of TAWSS has been chosen at approximately 2/3 of the range shown in the 3D plot

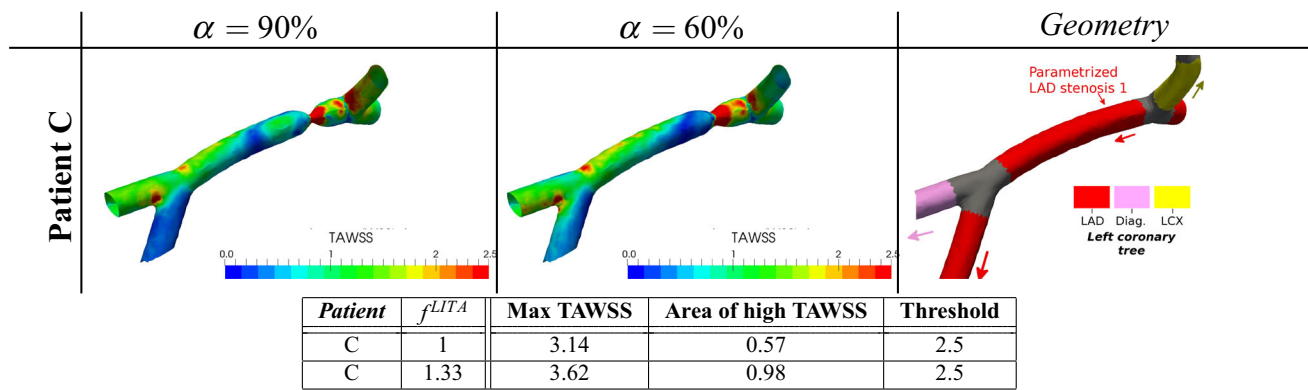


Fig. 18 Virtual scenario V, LAD–LCX and LAD–Diag bifurcations: comparison of TAWSS (Pa) for different inflow boundary conditions and stenosis. The table reports the maximum TAWSS (max TAWSS) and the area, computed in mm^2 , of the vessel characterized by high val-

ues of TAWSS (area of high TAWSS); the threshold (Threshold) used to identify high values of TAWSS has been chosen at maximum of the range shown in the 3D plot

are carried out and compared to reduced order simulations characterized by $N = 15$, $N = 75$ and $N = 150$ degrees of freedom, respectively. The error between high fidelity and reduced order solution is then computed. Figure 21 reports velocity, pressure and WSS relative errors over time (on the second cardiac cycle). H^1 norm is used for velocity error computation, L^2 norm for pressure error and L^∞ norm for WSS. The results show that the error is not constant in time. The reduced order model with $N = 15$ is not able to accurately predict the phenomena, resulting in peak relative errors of the order of 100%. However, increasing N to 75 or 150, relative errors decrease considerably over the entire time period. In particular, it is enough to consider $N = 150$ to obtain relative errors which are of the order of 0.2% on the velocity, less than 0.01% on the pressure and less than 1% on WSS, for all three values of θ . Moreover, Fig. 22 provides the same error analysis for $\theta = 45^\circ$ and two different values of the time step, obtained by considering both 80 time steps per cardiac cycle or 400 time steps per cardiac cycle. In both cases, $N = 150$ allows to obtain accurate approximation of the phenomena over the entire period. These results show that the proposed reduced order model provides accurate and fast simulations. Thus, in the following sections, we can employ the reduced model in place of the high-fidelity one without any significant loss of accuracy.

4.3 Discussion of the results of the virtual surgery platform for each scenario

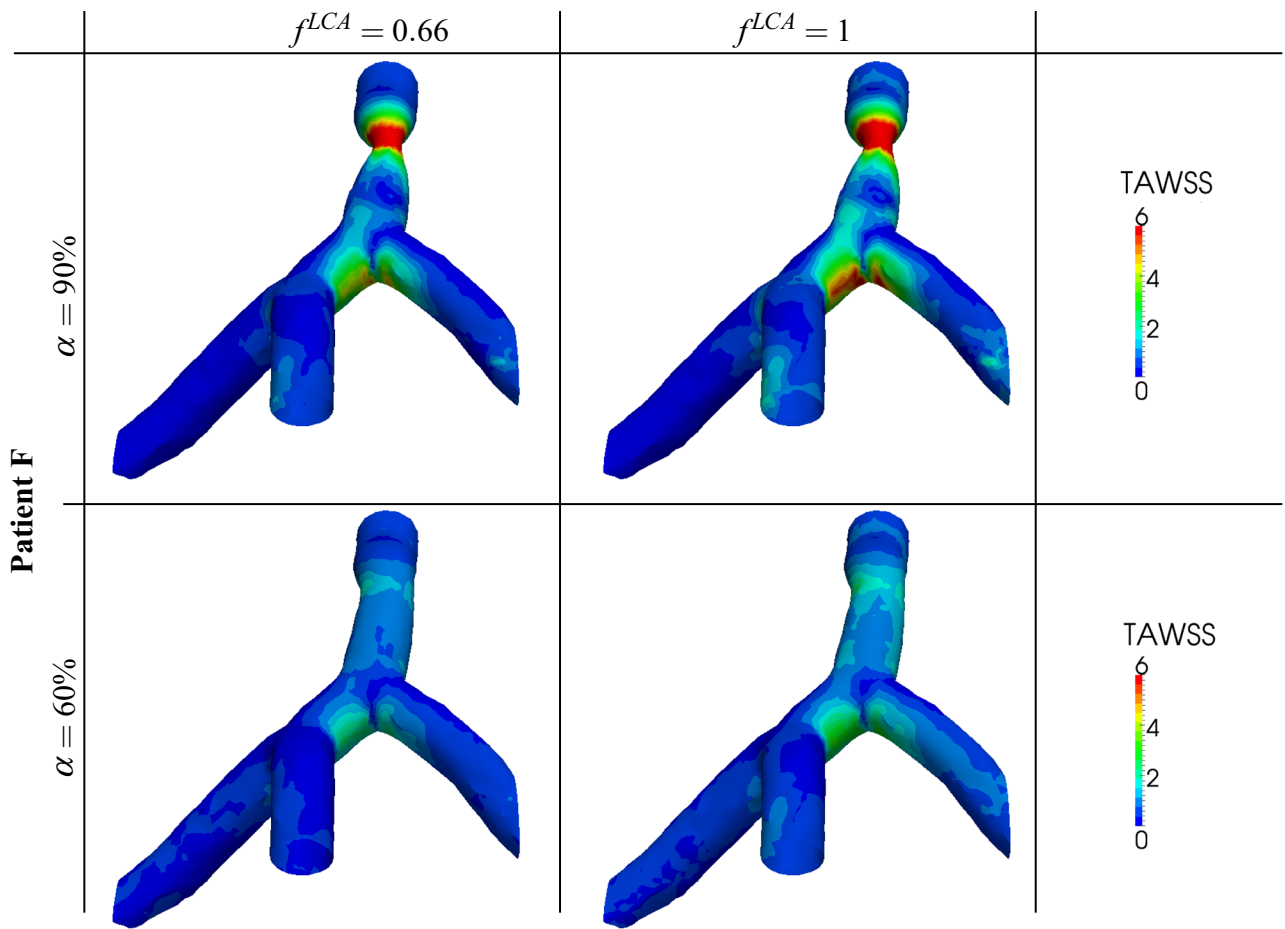
4.3.1 Virtual scenario I: effect of flow rate variation in Y-grafts

TAWSS results summarized in Fig. 7 (Y-graft with arterial graft) and Fig. 8 (Y-graft with venous graft) highlight the formation of a critical region, characterized by high TAWSS, on the LITA near the Y-graft. In all cases, a region of comparable

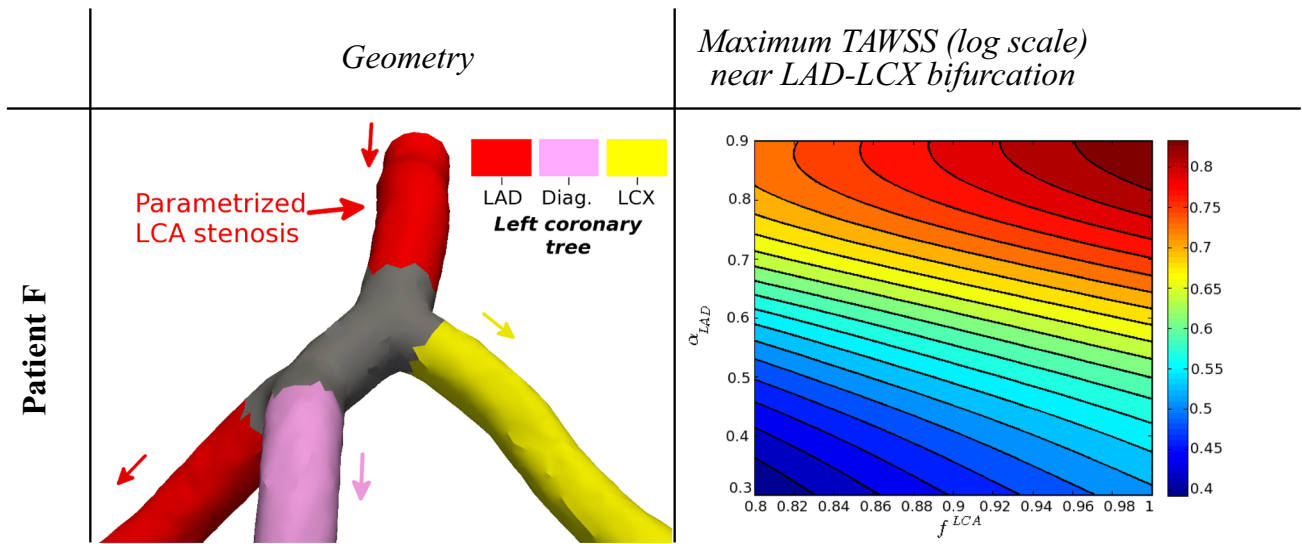
TAWSS is present also in the radial artery (see, in particular, Patient A) and SVG (see, in particular, Patient F), although the surface extension of the region of high TAWSS is larger in the LITA than in the other graft (see, in particular, Patients F and G). The region of high TAWSS is highly sensitive to the graft flow (f^{LITA}), and features a larger area increasing graft flow in all cases. Local geometrical features also influence the behavior of TAWSS: high values appear in the LITA graft proximally to the Y-graft where the graft features high curvature (see in particular Patients F, H, I). Moreover, maximum values of TAWSS are higher when the bifurcation angle between the two grafts is increased (compare Patient A to C, and Patient I to H).

4.3.2 Virtual scenario II: effect of flow rate variation in sequential grafts

Results in Fig. 9 highlight that, in all cases, a region of high TAWSS is found at the arterial beds of native coronary arteries, distal to the anastomosis. Moreover, in the case of cross-anastomosis (Patient A), the region of maximum WSS near the OM (first cross-anastomosis from the top) is slightly larger than the one near the LCX (second cross-anastomosis from the top). A similar behavior can be noticed in the flow case, where the latero-lateral anastomosis features higher WSS on the arterial bed than the termino-lateral anastomosis in Patient G, as in Patient C, where the first anastomosis is the most critical, as it features the highest WSS values, which gradually decrease at the remaining anastomoses. The magnitude of WSS on the arterial bed at the latero-lateral anastomosis is more sensible to increased graft flow rates in the flow direction case than the cross one. This is due to the fact that flow direction anastomosis of Patients C and G are supplied directly by LITA (where increased graft flow rate is enforced), while cross-anastomosis by radial artery of Patient A is only partially affected by the increased flow



(a)



(b)

Fig. 19 Virtual scenario V, LAD–LCX bifurcation: comparison of TAWSS (Pa) for different inflow boundary conditions and stenosis

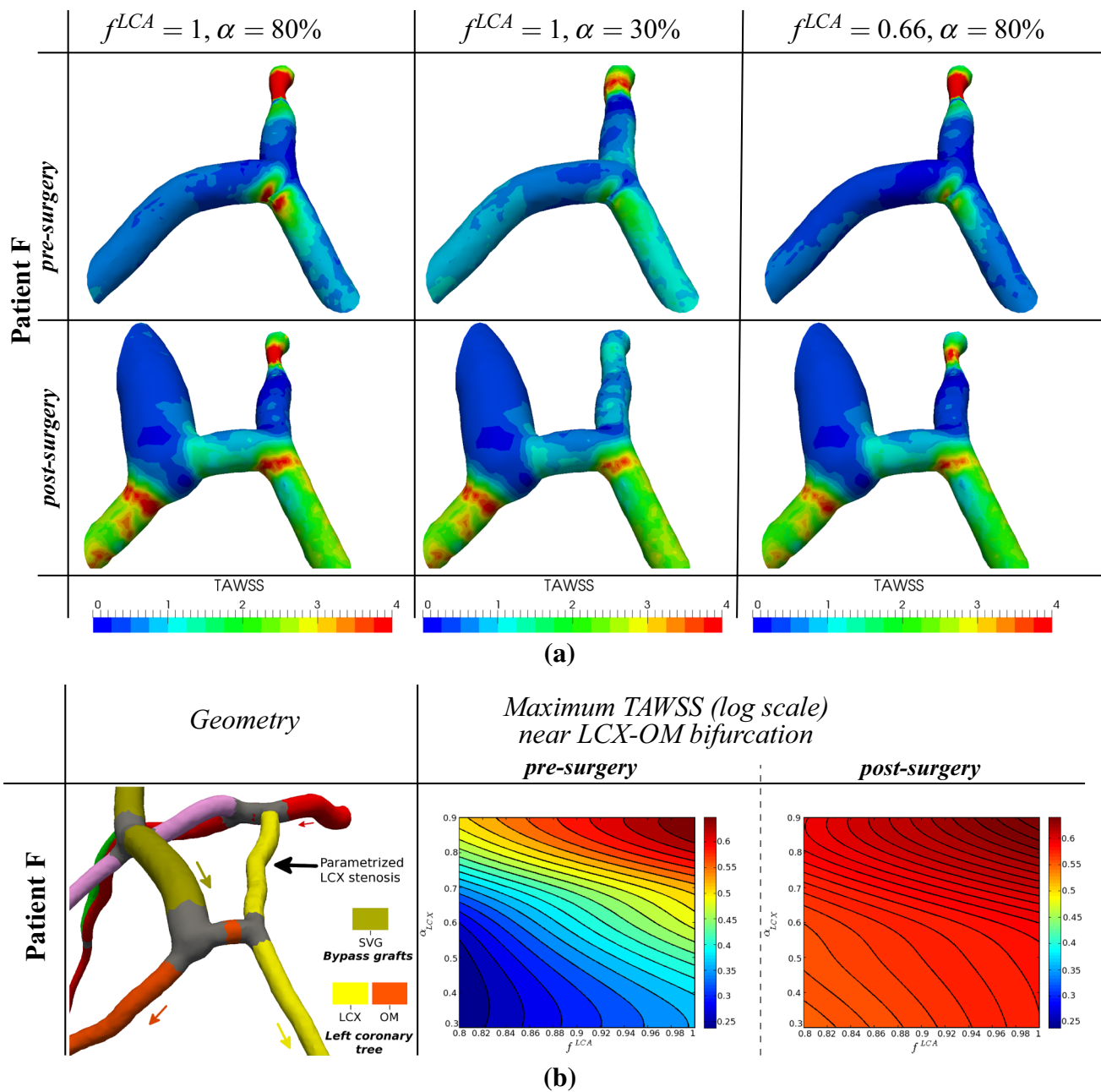


Fig. 20 Virtual scenario V, LCX–OM bifurcation: comparison of TAWSS (Pa), both pre- and post-surgery, for different inflow boundary conditions and stenosis

rate, because of the proximal flow split in the Y-graft between radial and LITA arteries.

4.3.3 Virtual scenario III: effect of flow rate and stenosis variation on anastomosis

We first consider anastomoses on the left coronary tree. Figure 10 shows the OSI near the anastomosis for different values of proximal stenosis (90, 80, 60, 0%) near a LITA-LAD end-to-side anastomosis. It is well agreed in the clinical

community that LITA is the gold standard for surgeries on the LAD, and that employing a LITA bypass graft on a non-critical stenosis may lead to early graft occlusion (Hillis and Smith 2011). The study on Patient B provides a numerical confirmation of the dependence of fluid dynamics indices on stenosis factors. OSI assumes its maximum values near the toe of the graft, and the size of the area of maximum OSI increases for decreasing proximal stenosis. This can be motivated by the higher residual flow in the LAD. This result is in agreement with the current clinical practice (Hillis and

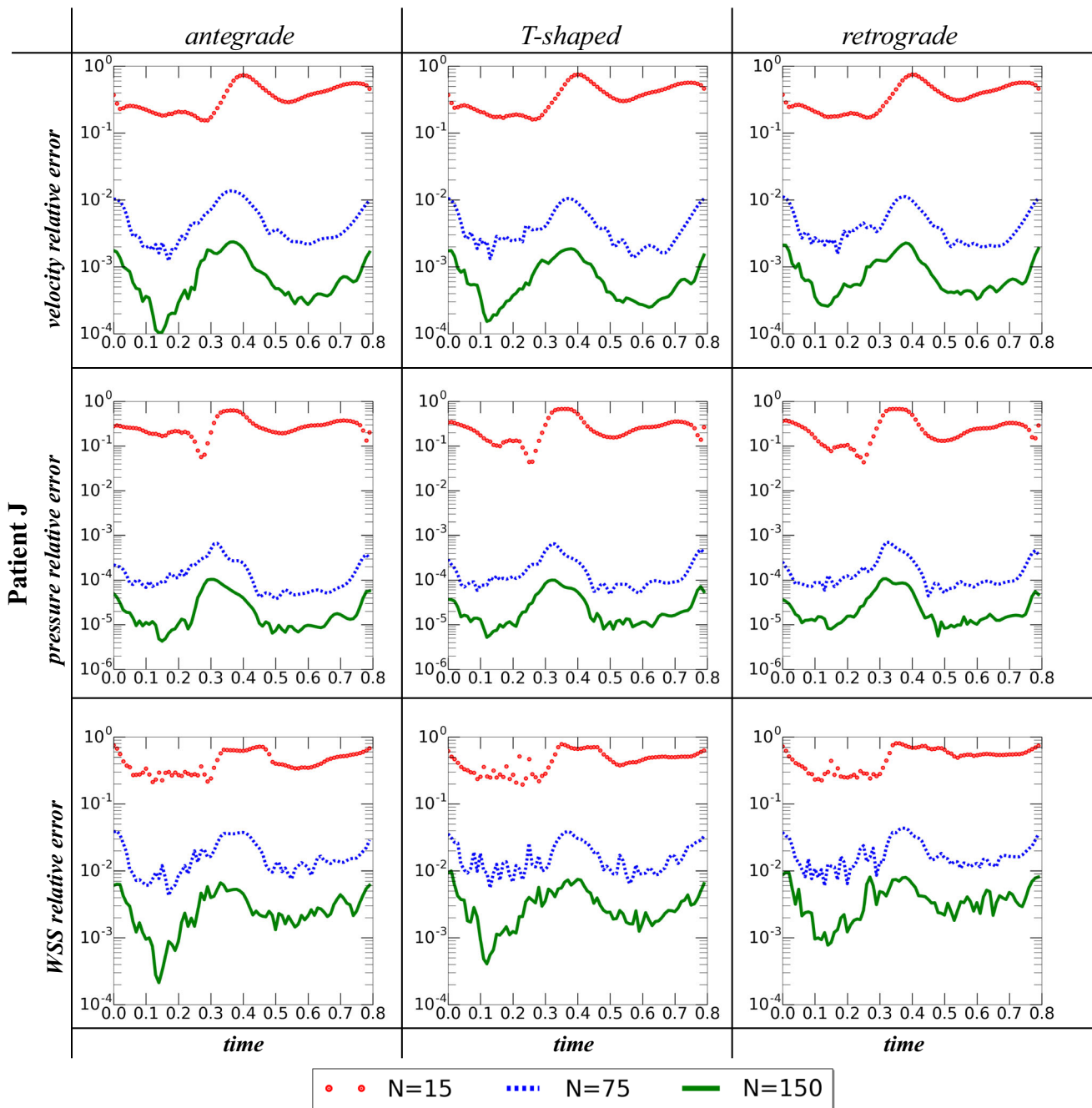


Fig. 21 Error analysis for the reduced order model over a cardiac cycle, considering three different values of the anastomosis parameter

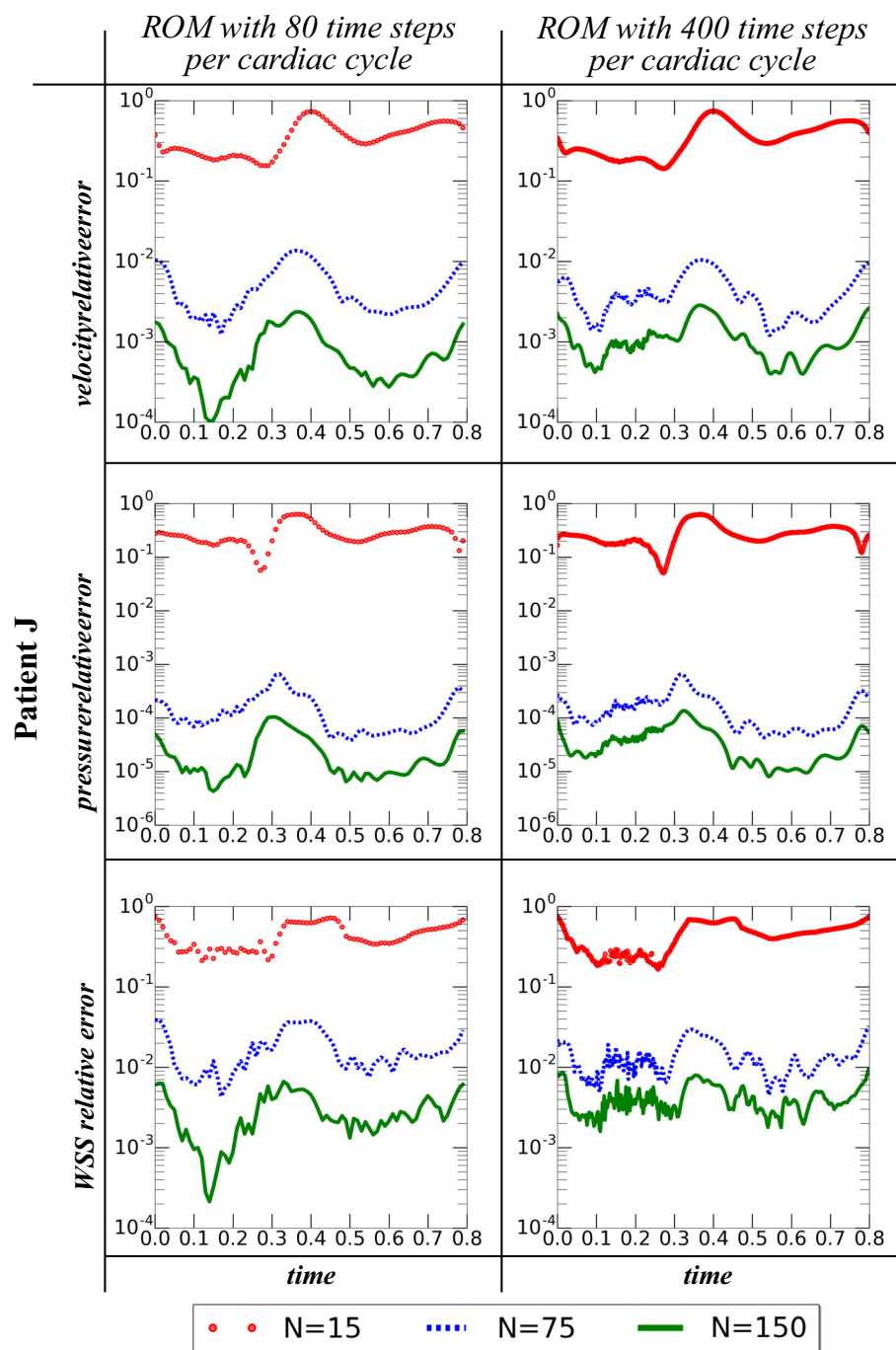
Smith 2011). Moreover, OSI assumes its maximum value in the LAD, proximal to the anastomosis, for all values of proximal stenosis.

Similar results are obtained for a more complete parameterization (on both flow rates and stenosis factors) on a more complex surgery (sequential LITA-Diag-LAD). Results in Fig. 11 show that parameterized flow rates do not have significant effects on the OSI for non-critical stenosis (second row). Instead, for more severe stenosis (first row), possible critical regions of the surgery, as highlighted by large values of

OSI, are located near the LITA-Diag anastomosis (especially for increased graft flow rates, first row, right) and proximally and distally to the stenosis (especially in the case of increased coronary flow rates, first row, middle).

Finally, we also consider the case of an arterial anastomosis on the right coronary network. Numerical results in Fig. 12 show that maximum WSS values, located near the heel of the graft, increases as the stenosis decreases: This is in agreement with the current clinical practice that prescribes the usage of radial artery as a graft only when stenosis is greater than 70%

Fig. 22 Error analysis for the reduced order model over a cardiac cycle, considering two different numbers of time steps per cardiac cycle



(Desai et al. 2004; Moran et al. 2001; Yie et al. 2008; Nicolini et al. 2014). This behavior does not depend strongly on the considered anastomosis (antegrade, T-shaped, retrograde).

4.3.4 Case IV: anastomosis variation

As in the previous section, we first compare different termino-lateral LITA-LAD anastomosis (left coronary network), corresponding to antegrade, T-shaped and retrograde anastomoses. Current clinical experience and anatomical

considerations suggest the use of antegrade anastomosis (Kirklin and Barratt-Boyes 1988). The results summarized in Figs. 13, 14 and 15 provide numerical evidence of this approach. Figure 13 shows a comparison of WSS distribution for the three anastomoses types and two different values of stenosis severity (critical: 90% and non-critical 60%). The results are provided for $t = 0.15$ s (peak LITA flow in systolic phase), since at this phase of the cardiac cycle the differences are more clearly visible. Both T-shaped and retrograde anastomoses feature worse patterns than the antegrade one since:

- (i) at the distal arterial floor, maximum WSS values in T-shaped and retrograde cases are approximately two times higher than in the antegrade case. This pattern remains unchanged for different stenosis severities;
- (ii) intermediate WSS values are also observed in the proximal part of the arterial floor. This region is larger for T-shaped and retrograde anastomoses than the antegrade, although minimum and maximum value are not affected by the anastomosis type. Moreover, this region enlarges as the degree of proximal stenosis decreases, because of the higher residual flow in the native coronary;
- (iii) in all anastomoses, the region downstream to the toe features low WSS.

The analysis of transversal velocity profiles (normalized by the maximum velocity in the anastomosis, at the same time) is carried out in Fig. 14, at $t = 0.15$ s (peak LITA flow in systolic phase) and $t = 0.55$ s (peak LCA flow in diastolic phase). In all anastomoses, Dean vortices appear in the region of the anastomosis. Peak values of transversal velocity are reached at $t = 0.55$ s. In agreement with the previous discussion, both T-shaped and retrograde anastomoses feature worse patterns than the antegrade one since:

- (i) Dean vortices are dissipated more quickly in the antegrade anastomosis than in T-shaped and retrograde ones;
- (ii) antegrade anastomosis features lower transversal than both T-shaped and retrograde anastomoses in the section closest to the anastomosis. At $t = 0.15$ s T-shaped anastomosis features the highest transversal velocity, while a similar behavior among T-shaped and retrograde cases is observed for $t = 0.55$ s;
- (iii) a third vortex may be formed in retrograde anastomosis, especially for high stenosis and a peak LITA flow. This is particularly apparent in the second slice on the third row of Fig. 14.

Moreover, Fig. 15 shows a comparison of the pressure drop in the three different anastomoses. The pressure drop is minimum for antegrade anastomosis; T-shaped and retrograde anastomoses feature instead an higher pressure drop. Moreover, an higher pressure drop across the anastomosis is obtained decreasing the stenosis severity; this is an additional confirmation of the clinical experience that a CABG surgery should be performed only for critical stenoses.

A different behavior can be observed instead when considering a venous, rather than a LITA graft, on the right coronary tree. Vein grafts are usually characterized by a larger radius. In particular, Fig. 16 reports a comparison of WSS at different phases of the cardiac cycle for three anastomoses types, highlighting that T-shaped anastomosis feature comparable

patterns to antegrade anastomosis. Also in this case, the result is in good agreement with current clinical practice, which prescribes the use of T-shaped grafts due to anatomical considerations (Kirklin and Barratt-Boyes 1988). Our numerical results show that, in the retrograde case, maximum values of WSS are observed on the lateral arterial surface distal to the anastomosis and near the toe of the graft. The WSS magnitude in these regions is almost twice the magnitude in the antegrade and T-shaped cases.

4.3.5 Virtual scenario V: effect of flow rate and stenosis variation on native coronary bifurcations

Since the aim of this work is mainly related to the study of bypass grafts, in the previous sections we focused our attention only on anastomoses. However, similar studies can be carried out on native coronary bifurcations as well, which are also possible critical regions (before and) after the surgery. Thanks to capability to perform parameterized evaluations through the reduced order model it is possible to consider several different coronary artery flow rates, corresponding to either standard ($f^{LCA} = 1$), increased ($f^{LCA} = 1.33$) or decreased ($f^{LCA} = 0.8$) flow rates, or different stenosis severity, either critical ($\alpha_{LAD} = 80\%$) or non-critical ($\alpha_{LAD} = 30\%$). Critical regions, characterized by high WSS, are present at the bifurcations in all considered cases (LAD-Diag bifurcation for Patient I in Fig. 17, LAD-LCX and LAD-Diag for Patient C in Fig. 18, and LAD-LCX for Patient F in Fig. 19). For instance, the effect of increased LCA flow rates is visible for Patient I at the LAD-Diag bifurcation; this is related to the presence of locally higher WSS at the LAD wall both proximally and distally the bifurcation. The arterial wall near the bifurcation features high WSS also in Patient F (Fig. 19); maximum WSS values are influenced both by the inlet flow rate at the LCA ostium and the severity of the LCA stenosis. In fact, lower values of the former parameter cause a smaller region of high WSS (compare Fig. 19a by row). Moreover, the impingement of the jet of high velocity, caused by critical stenosis, on the arterial wall, is an additional cause of higher WSS (compare Fig. 19a by column). Finally, we provide a plot of the maximum WSS for a wide range of stenosis severity and inlet flow rates in Fig. 19b; being able to query almost inexpensively our reduced order framework is the cornerstone in order to perform the analysis yielding this plot, that would have otherwise required several weeks of computational times if relying on traditional high-fidelity techniques.

A similar study can also be performed both before and after the surgery. In particular, we summarize in Fig. 20 the results for the LCX-OM bifurcation of Patient F, which, in the post-surgical stage, is also perfused and affected by the blood flow from a saphenous vein graft. The results in Fig. 20a compare the WSS near the bifurcation for criti-

cal stenosis ($\alpha_{LAD} = 80\%$) and standard native coronary flow ($f^{LCA} = 1$), non-critical stenosis ($\alpha_{LAD} = 30\%$) and standard ($f^{LCA} = 1$) native coronary flow, critical stenosis and decreased ($f^{LCA} = 0.8$) native coronary flow. The pattern of WSS at the bifurcation before the surgery, summarized in Fig. 20b, is similar to the one at the LAD-LCX bifurcation of the same patient (discussed in the previous section), although smaller values of WSS are identified. On the other hand, after the surgery maximum values of WSS are less sensible to LCA inlet flow rate and stenosis factors. This is motivated by the fact that, in this case, the SVG graft is the main source of blood flow for both LCX and OM branches.

5 Conclusions

In this work we have taken advantage of a reduced order computational framework first proposed in (Ballarin et al. 2016) for the study of the hemodynamics in several patient-specific coronary artery bypass grafts (CABGs). The main aim of this work is to handle in a fast and efficient way simulations on (i) patient-specific geometries, (ii) characterized by different parameters and (iii) employing reduced order models to cut down large computational costs. The clinical dataset we employed features a large variability on diseased coronary arteries and bypass grafts. For the sake of comparison between different scenarios (related to either blood flow rates, disease or surgery choices) on the same patient-specific configuration, a parameterized formulation has been introduced. Several numerical results and parametric analyses have been provided. In particular,

- I. the comparison of different Y-graft has highlighted different behaviors for radial and saphenous vein grafts (lower WSS on the former), and the presence of critical regions especially near the Y-graft for increased flow rates;
- II. in a similar way, critical regions near the arterial bed are detected in case of sequential anastomoses;
- III. surgery outcomes for different stenosis in native coronary arteries have been studied; the obtained results are in good agreement with clinical practice that prescribes to undergo surgery only for critical stenoses. In particular, we have analyzed a LITA-LAD anastomosis, showing that a larger region of high oscillatory shear index appears near the toe of the graft if the stenosis is not critical, and a radial-PL anastomosis, showing that increased wall shear stress is present near the heel of the graft for non-critical stenosis;
- IV. variation of anastomosis, either of LITA-LAD or SVG-PDA anastomoses, has been discussed. The results

of our virtual surgery framework are in agreement with current clinical practice that suggests the use of antegrade anastomoses in LITA-LAD and the use of T-shaped anastomoses on the right coronary tree. These conclusions have been obtained performing comparison of WSS, transversal velocity profiles and pressure drop for three different anastomosis configurations, representative of antegrade, T-shaped and retrograde-flow anastomoses;

- V. finally, the proposed framework has been exploited for evaluating flow patterns at native coronary artery bifurcations, also performing a comparison before and after surgery.

The proposed virtual surgery platform exploits a model reduction framework, capable of automatically handling physical and geometrical parameters, to numerically obtain quantities of interest in a very fast way (order of few minutes on a laptop). This can represent an attractive platform for the rapid study of complex CABG networks that frequently occur in the clinical practice. Future improvements on the mathematical modeling will involve more accurate outflow boundary conditions. As a matter of fact, in view of a better personalization of the study, multiscale lumped parameters models (Kim et al. 2010; Sankaran et al. 2012; Ramachandra et al. 2016; Sankaran et al. 2016), properly interfaced with available patient-specific clinical data (ventricular volumes, ventricular pressures, etc.) should be used. Further improvement on the computational reduction techniques may be obtained by incorporating design of experiment into the proposed framework (Tran et al. 2017; Schiavazzi et al. 2017), in place of a random selection over the parameter space as done in the present work.

Acknowledgements We acknowledge the use of CINECA supercomputing facilities within the projects “Convenzione di Ateneo” agreement between Politecnico di Milano and CINECA, and “COGESTRA” between SISSA and CINECA, and Istituto Nazionale di Fisica Nucleare, within the project SUMA. We acknowledge the use of a customized version of the library `rb00mit` within `libMesh` (Knezevic and Peterson 2011; Kirk et al. 2006) for the numerical simulations, and of the Vascular Modelling Toolkit `vmtk` (Antiga et al. 2008) and `3DSlicer` (Fedorov et al. 2012) for the medical imaging pipeline.

Compliance with ethical standards

Funding Francesco Ballarin and Elena Faggiano acknowledge the support of the PRIN project “Mathematical and numerical modeling of the cardiovascular system, and their clinical applications”. Gianluigi Rozza acknowledges the SISSA Excellence Grant NOFYSAS “Computational and Geometrical Reduction Strategies for the simulation, control and optimization of complex systems”. We also acknowledge ERC Advanced Grant Mathcard (Number 227058).

Conflict of Interest The authors declare that they have no conflict of interest.

References

- Antiga L (2002) Patient-Specific modeling of geometry and blood flow in large arteries. PhD thesis, Dipartimento di Bioingegneria, Politecnico di Milano
- Antiga L, Ene-Iordache B, Remuzzi A (2003) Computational geometry or patient-specific reconstruction and meshing of blood vessels from MR and CT angiography. *IEEE Trans Med Imaging* 22(5):674–684
- Antiga L, Piccinelli M, Botti L, Ene-Iordache B, Remuzzi A, Steinman D (2008) An image-based modeling framework for patient-specific computational hemodynamics. *Med Biol Eng Comput* 46:1097–1112
- Ballarin F (2015) Reduced-order models for patient-specific haemodynamics of coronary artery bypass grafts. PhD thesis, Department of Mathematics, Politecnico di Milano. <http://hdl.handle.net/10589/102804>
- Ballarin F, Faggiano E, Ippolito S, Manzoni A, Quarteroni A, Rozza G, Scrofani R (2016) Fast simulations of patient-specific haemodynamics of coronary artery bypass grafts based on a POD-Galerkin method and a vascular shape parametrization. *J Comput Phys* 315:609–628
- Ballarin F, Manzoni A, Quarteroni A, Rozza G (2015) Supremizer stabilization of POD-Galerkin approximation of parametrized steady incompressible Navier-Stokes equations. *Int J Numer Methods Eng* 102(5):1136–1161
- Berkooz G, Holmes P, Lumley J (1993) The proper orthogonal decomposition in the analysis of turbulent flows. *Annu Rev Fluid Mech* 25(1):539–575
- Bertolotti C, Deplano V (2000) Three-dimensional numerical simulations of flow through a stenosed coronary bypass. *J Biomech* 33(8):1011–1022
- Bertolotti C, Deplano V, Fuseri J, Dupouy PJ (2001) Numerical and experimental models of post-operative realistic flows in stenosed coronary bypasses. *J Biomech* 34(8):1049–1064
- Bishop RL (1975) There is more than one way to frame a curve. *Am Math Mon* 82(3):246–251
- Bonert M, Myers JG, Fremes S, Williams J, Ross Ethier C (2002) A numerical study of blood flow in coronary artery bypass graft side-to-side anastomoses. *Ann Biomed Eng* 30(5):599–611
- Boutsianis E, Dave H, Frauenfelder T, Poulikakos D, Wildermuth S, Turina M, Ventikos Y, Zund G (2004) Computational simulation of intracoronary flow based on real coronary geometry. *Eur J Cardio-Thorac Surg* 26(2):248–256
- Burkardt J, Gunzburger M, Lee H-C (2006) POD and CVT-based reduced-order modeling of Navier–Stokes flows. *Comput Methods Appl Mech Eng* 196(1–3):337–355
- Chaichana T, Sun Z, Jewkes J (2011) Computation of hemodynamics in the left coronary artery with variable angulations. *J Biomech* 44(10):1869–1878
- Chen J, Lu X-Y, Wang W (2006) Non-newtonian effects of blood flow on hemodynamics in distal vascular graft anastomoses. *J Biomech* 39(11):1983–1995
- Deplano V, Bertolotti C, Boiron O (2001) Numerical simulations of unsteady flows in a stenosed coronary bypass graft. *Med Biol Eng Comput* 39(4):488–499
- Desai ND, Cohen EA, Naylor CD, Fremes SE (2004) A randomized comparison of radial-artery and saphenous-vein coronary bypass grafts. *N Engl J Med* 351(22):2302–2309
- Do H, Owida AA, Yang W, Morsi YS (2011) Numerical simulation of the haemodynamics in end-to-side anastomoses. *Int J Numer Methods Fluids* 67:638–650
- Dur O, Coskun S, Coskun K, Frakes D, Kara L, Pekkan K (2011) Computer-aided patient-specific coronary artery graft design improvements using CFD coupled shape optimizer. *Cardiovasc Eng Technol* 2:35–47
- Fedorov A, Beichel R, Kalpathy-Cramer J, Finet J, Fillion-Robin J-C, Pujol S, Bauer C, Jennings D, Fennessy F, Sonka M, Buatti J, Aylward S, Miller JV, Pieper S, Kikinis R (2012) 3D Slicer as an image computing platform for the quantitative imaging network. *Magn Reson Imaging* 30(9):1323–1341
- Fei D-Y, Thomas JD, Rittgers SE (1994) The effect of angle and flow rate upon hemodynamics in distal vascular graft anastomoses: a numerical model study. *J Biomech Eng* 116(3):331–336
- Frangi AF, Niessen WJ, Vincken KL, Viergever MA (1998) Multi-scale vessel enhancement filtering. In: Wells WM, Colchester A, Delp S (eds) *Medical image computing and computer-assisted intervention—MICCAI'98*, vol 1496., lecture notes in computer science. Springer, Berlin Heidelberg, pp 130–137
- Frauenfelder E, Schertler T, Husmann L, Leschka S, Poulikakos D, Marincek B, Alkadhi H (2007) Flow and wall shear stress in end-to-side and side-to-side anastomosis of venous coronary artery bypass grafts. *Biomed Eng OnLine* 6(1):35:1–35:13
- Freshwater IJ, Morsi YS, Lai T (2006) The effect of angle on wall shear stresses in a LIMA to LAD anastomosis: numerical modelling of pulsatile flow. *Proc Inst Mech Eng Part H J Eng Med* 220(7):743–757
- Ghista D, Kabinejadian F (2013) Coronary artery bypass grafting hemodynamics and anastomosis design: a biomedical engineering review. *Biomed Eng Online* 12(1):129:1–129:28
- Gijzen F, Allanic E, van de Vosse F, Janssen J (1999) The influence of the non-newtonian properties of blood on the flow in large arteries: unsteady flow in a 90° curved tube. *J Biomech* 32(7):705–713
- Giordana S, Sherwin S, Peiró J, Doorly D, Crane J, Lee K, Cheshire N, Caro C (2005) Local and global geometric influence on steady flow in distal anastomoses of peripheral bypass grafts. *J Biomech Eng* 127:1087
- Go AS, Mozaffarian D, Roger VL, Benjamin EJ, Berry JD, Blaha MJ, Dai S, Ford ES et al (2014) Executive summary: heart disease and stroke statistics-2014 update: a report from the American Heart Association. *Circulation* 129(3):399–410
- Guerciotti B, Vergara C, Ippolito S, Quarteroni A, Antona C, Scrofani R (2016) Computational study of the risk of restenosis in coronary bypasses. *Biomech Model Mechanobiol* 16(1):313–332
- Hesthaven JS, Rozza G, Stamm B (2016) Certified reduced basis methods for parametrized partial differential equations. Springer briefs in mathematics. Springer International Publishing, New York
- Hillis LD, Smith PK et al (2011) 2011 ACCF/AHA guideline for coronary artery bypass graft surgery—a report of the American College of Cardiology Foundation/American Heart Association task force on practice guidelines developed in collaboration with the american association for thoracic surgery, society of cardiovascular anesthesiologists, and society of thoracic surgeons. *J Am Coll Cardiol* 58(24):e123–e210
- Idu MM, Buth J, Hop WCJ, Cuypers P, van de Pavoordt EDWM, Tor-doir JMH (1999) Factors influencing the development of vein-graft stenosis and their significance for clinical management. *Eur J Vasc Endovasc Surg* 17(1):15–21
- Inzoli F, Migliavacca F, Pennati G (1996) Numerical analysis of steady flow in aorto-coronary bypass 3-D model. *J Biomech Eng* 118(2):172–179
- Ishida N, Sakuma H, Cruz BP, Shimono T, Tokui T, Yada I, Takeda K, Higgins CB (2001) MR flow measurement in the internal mammary artery-to-coronary artery bypass graft: comparison with graft stenosis at radiographic angiography. *Radiology* 220(2):441–447
- Jackson ZS, Ishibashi H, Gotlieb AI, Langille BL (2001) Effects of anastomotic angle on vascular tissue responses at end-to-side arterial grafts. *J Vasc Surg* 34(2):300–307

- Kabinejadian F, Chua L, Ghista D, Sankaranarayanan M, Tan Y (2010) A novel coronary artery bypass graft design of sequential anastomoses. *Ann Biomed Eng* 38(10):3135–3150
- Kabinejadian F, Ghista DN (2012) Compliant model of a coupled sequential coronary arterial bypass graft: effects of vessel wall elasticity and non-Newtonian rheology on blood flow regime and hemodynamic parameters distribution. *Med Eng Phys* 34(7):860–872
- Keegan J, Gatehouse PD, Yang G-Z, Firmin DN (2004) Spiral phase velocity mapping of left and right coronary artery blood flow: correction for through-plane motion using selective fat-only excitation. *J Magn Reson Imaging* 20(6):953–960
- Keynton RS, Shu MCS, Rittgers SE (1991) The effect of angle and flow rate upon hemodynamics in distal vascular graft anastomoses: an in vitro model study. *J Biomech Eng* 113(4):458–463
- Kim HJ, Vignon-Clementel IE, Figueroa CA, Jansen KE, Taylor CA (2010) Developing computational methods for three-dimensional finite element simulations of coronary blood flow. *Finite Elements Anal Des* 46(6):514–525
- Kirk BS, Peterson JW, Stogner RH, Carey GF (2006) libMesh: a C++ library for parallel adaptive mesh refinement/coarsening simulations. *Eng Comput* 22(3–4):237–254
- Kirklin JW, Barratt-Boyes BG (1988) *Cardiac surgery: morphology, diagnostic criteria, natural history, techniques, results, and indications*. Churchill Livingstone, New York
- Kleinstreuer C, Nazemi M, Archie JP (1991) Hemodynamics analysis of a stenosed carotid bifurcation and its plaque-mitigating design. *J Biomech Eng* 113(3):330–335
- Knezevic DJ, Peterson JW (2011) A high-performance parallel implementation of the certified reduced basis method. *Comput Methods Appl Mech Eng* 200(13–16):1455–1466
- Ku DN, Giddens DP, Zarins CK, Glagov S (1985) Pulsatile flow and atherosclerosis in the human carotid bifurcation. Positive correlation between plaque location and low oscillating shear stress. *Arterioscler Thromb Vasc Biol* 5(3):293–302
- Kute SM, Vorp DA (2001) The effect of proximal artery flow on the hemodynamics at the distal anastomosis of a vascular bypass graft: computational study. *J Biomech Eng* 123(3):277–283
- Lei M, Archie JP, Kleinstreuer C (1997) Computational design of a bypass graft that minimizes wall shear stress gradients in the region of the distal anastomosis. *J Vasc Surg* 25(4):637–646
- Lei M, Giddens DP, Jones SA, Loth F, Bassiouny H (2000) Pulsatile flow in an end-to-side vascular graft model: comparison of computations with experimental data. *J Biomech Eng* 123(1):80–87
- Lorensen WE, Cline HE (1987) Marching cubes: a high resolution 3d surface construction algorithm. *Comput Graph* 21(4):163–169
- Loth F, Fischer PF, Bassiouny HS (2008) Blood flow in end-to-side anastomoses. *Annu Rev Fluid Mech* 40:367–393
- Manzoni A (2014) An efficient computational framework for reduced basis approximation and a posteriori error estimation of parametrized Navier–Stokes flows. *ESAIM Math Model Numer Anal* 48:1199–1226
- Marsden AL (2014) Optimization in cardiovascular modeling. *Annu Rev Fluid Mech* 46(1):519–546
- Marsden AL, Feinstein JA, Taylor CA (2008) A computational framework for derivative-free optimization of cardiovascular geometries. *Comput Methods Appl Mech Eng* 197(21–24):1890–1905
- Migliavacca F, Dubini G (2005) Computational modeling of vascular anastomoses. *Biomech Model Mechanobiol* 3(4):235–250
- Moran SV, Baeza R, Guarda E, Zalaquett R, Irrarrazaval MJ, Marchant E, Deck C (2001) Predictors of radial artery patency for coronary bypass operations. *Ann Thorac Surg* 72(5):1552–1556
- Nicolini F, Agostinelli A, Spaggiari I, Vezzani A, Benassi F, Maestri F, Gherli T (2014) Current trends in surgical revascularization of multivessel coronary artery disease with arterial grafts. *Int Heart J* 55(5):381–385
- Nordgaard H, Swillens A, Nordhaug D, Kirkeby-Garstad I, Van Loo D, Vitale N, Segers P, Haaverstad R, Lovstakken L (2010) Impact of competitive flow on wall shear stress in coronary surgery: computational fluid dynamics of a LIMA-LAD model. *Cardiovasc Res* 88(3):512–519
- Owida AA, Do H, Morsi YS (2012) Numerical analysis of coronary artery bypass grafts: an over view. *Comput Methods Program Biomed* 108(2):689–705
- Pagni S, Storey J, Ballen J, Montgomery W, Qaqish NK, Etoch S, Spence PA (1997) Factors affecting internal mammary artery graft survival: how is competitive flow from a patent native coronary vessel a risk factor? *J Surg Res* 71(2):172–178
- Perona P, Malik J (1990) Scale-space and edge detection using anisotropic diffusion. *IEEE Trans Pattern Anal Mach Intell* 12(7):629–639
- Politis AK, Stavropoulos GP, Christolis MN, Panagopoulos PG, Vlachos NS, Markatos NC (2008) Numerical modelling of simulated blood flow in idealized composite arterial coronary grafts: transient flow. *J Biomech* 41(1):25–39
- Probst M, Lülfsmann M, Nicolai M, Bücken HM, Behr M, Bischof CH (2010) Sensitivity of optimal shapes of artificial grafts with respect to flow parameters. *Comput Methods Appl Mech Eng* 199(17–20):997–1005
- Puskas JD, Lazar HL, Mack MJ, Sabik JF III, Taggart DP (2014) State-of-the-art coronary artery bypass graft. *Semin Thorac Cardiovasc Surg* 26(1):76–94
- Qiao A, Liu Y (2006) Influence of graft-host diameter ratio on the hemodynamics of CABG. *Bio-Med Mater Eng* 16(3):189–201
- Quarteroni A, Manzoni A, Negri F (2016) *Reduced Basis Methods for partial differential equations. An introduction, volume 92 of unitext*. Springer, New York
- Ramachandra AB, Kahn AM, Marsden AL (2016) Patient-specific simulations reveal significant differences in mechanical stimuli in venous and arterial coronary grafts. *J Cardiovasc Transl Res* 9(4):279–290
- Ravindran S (2000) A reduced-order approach for optimal control of fluids using proper orthogonal decomposition. *Int J Numer Methods Fluids* 34:425–448
- Ross Ethier C, Steinman DA, Zhang X, Karpik S, Ojha M (1998) Flow waveform effects on end-to-side anastomotic flow patterns. *J Biomech* 31(7):609–617
- Rowe GG, Thomsen JH, Stenlund RR, McKenna DH, Sialer S, Corliss RJ (1969) A study of hemodynamics and coronary blood flow in man with coronary artery disease. *Circulation* 39(1):139–148
- Rozza G, Huynh DBP, Manzoni A (2013) Reduced basis approximation and a posteriori error estimation for Stokes flows in parametrized geometries: roles of the inf-sup stability constants. *Numer Math* 125(1):115–152
- Sabik JF III, Blackstone EH (2008) Coronary artery bypass graft patency and competitive flow. *J Am Coll Cardiol* 51(2):126–128
- Sabik JF III, Lytle BW, Blackstone EH, Houghtaling PL, Cosgrove DM (2005) Comparison of saphenous vein and internal thoracic artery graft patency by coronary system. *Ann Thorac Surg* 79(2):544–551
- Sabik JF III, Lytle BW, Blackstone EH, Khan M, Houghtaling PL, Cosgrove DM (2003) Does competitive flow reduce internal thoracic artery graft patency? *Ann Thorac Surg* 76(5):1490–1497
- Sankaran S, Esmaily Moghadam M, Kahn A, Tseng E, Guccione J, Marsden A (2012) Patient-specific multiscale modeling of blood flow for coronary artery bypass graft surgery. *Ann Biomed Eng* 40:2228–2242
- Sankaran S, Kim HJ, Choi G, Taylor CA (2016) Uncertainty quantification in coronary blood flow simulations: impact of geometry, boundary conditions and blood viscosity. *J Biomech* 49(12):2540–2547 (Cardiovascular Biomechanics in Health and Disease)

- Sankaran S, Marsden AL (2010) The impact of uncertainty on shape optimization of idealized bypass graft models in unsteady flow. *Phys Fluids* 22(12):1–16
- Schiavazzi D, Doostan A, Iaccarino G, Marsden A (2017) A generalized multi-resolution expansion for uncertainty propagation with application to cardiovascular modeling. *Comput Methods Appl Mech Eng* 314:196–221
- Sherwin SJ, Doorly DJ (2003) Flow dynamics within model distal arterial bypass grafts. *Adv Fluid Mech* 34:327–374
- Sherwin SJ, Shah O, Doorly DJ, Peiro J, Papaharilaou Y, Watkins N, Caro CG, Dumoulin CL (1999) The influence of out-of-plane geometry on the flow within a distal end-to-side anastomosis. *J Biomech Eng* 122(1):86–95
- Si H (2015) Tetgen, a delaunay-based quality tetrahedral mesh generator. *ACM Trans Math Softw* 41(2):11:1–11:36
- Staalsen N-H, Ulrich M, Winther J, Pedersen EM, How T, Nygaard H (1995) The anastomosis angle does change the flow fields at vascular end-to-side anastomoses in vivo. *J Vasc Surg* 21(3):460–471
- Swillens A, De Witte M, Nordgaard H, Løvstakken L, Van Loo D, Trachet B, Vierendeels J, Segers P (2012) Effect of the degree of LAD stenosis on “competitive flow” and flow field characteristics in LIMA-to-LAD bypass surgery. *Med Biol Eng Comput* 50(8):839–849
- Taylor CA, Draney MT (2004) Experimental and computational methods in cardiovascular fluid mechanics. *Ann Rev Fluid Mech* 36:197–231
- Towne JB, Schmitt DD, Seabrook GR, Bandyk DF (1991) The effect of vein diameter on patency of in situ grafts. *J Cardiovasc Surg* 32(2):192–196
- Tran JS, Schiavazzi DE, Ramachandra AB, Kahn AM, Marsden AL (2017) Automated tuning for parameter identification and uncertainty quantification in multi-scale coronary simulations. *Comput Fluids* 142:128–138
- Wen J, Zheng T, Jiang W, Deng X, Fan Y (2011) A comparative study of helical-type and traditional-type artery bypass grafts: numerical simulation. *Am Soc Artif Intern Organs J* 57(5):399–406
- Xiong FL, Chong CK (2008) A parametric numerical investigation on haemodynamics in distal coronary anastomoses. *Med Eng Phys* 30(3):311–320
- Yie K, Na C-Y, Oh SS, Kim J-H, Shinn S-H, Seo H-J (2008) Angiographic results of the radial artery graft patency according to the degree of native coronary stenosis. *Eur J Cardio-Thorac Surg* 33(3):341–348
- Zhang J-M, Chua LP, Ghista DN, Yu SCM, Tan YS (2008) Numerical investigation and identification of susceptible sites of atherosclerotic lesion formation in a complete coronary artery bypass model. *Med Biol Eng Comput* 46(7):689–699
- Zhang J-M, Luo T, Tan SY, Lomarda AM, Wong ASL, Keng FYJ, Allen JC, Huo Y, Su B, Zhao X, Wan M, Kassab GS, Tan RS, Zhong L (2015) Hemodynamic analysis of patient-specific coronary artery tree. *Int J Numer Methods Biomed Eng* 31(4):1–16
- Zhang J-M, Zhong L, Luo T, Lomarda AM, Huo Y, Yap J, Lim ST, Tan RS, Wong ASL, Tan JWC, Yeo KK, Fam JM, Keng FYJ, Wan M, Su B, Zhao X, Allen JC, Kassab GS, Chua TSJ, Tan SY (2016) Simplified models of non-invasive fractional flow reserve based on ct images. *PLoS ONE* 11(5):1–20